

DEFINING A FAILURE SURFACE FOR FFF PARTS USING A NOVEL FAILURE CRITERION

Gerardo A. Mazzei Capote

A thesis submitted in partial fulfillment of
the requirements for the degree of

**Master of Science
(Mechanical Engineering)**

at the

UNIVERSITY OF WISCONSIN-MADISON

2018

Final Oral Examination: September 7th, 2018

Approval

The following thesis, **Defining a failure surface for FFF parts using a novel failure criterion**, developed at the **University of Wisconsin-Madison** has been approved by:

Signature

Date

Professor Tim A. Osswald
Department of Mechanical Engineering
College of Engineering
University of Wisconsin-Madison

Abstract

Fused Filament Fabrication (FFF) is arguably the most widely available Additive Manufacturing technology at the moment. Offering the possibility of producing complex geometries in a compressed product development cycle and in a plethora of materials, it comes as no surprise that FFF is attractive to multiple industries, including the automotive and aerospace segments. However, the high anisotropy of parts developed through this technique implies that part failure prediction is extremely difficult —a requirement that must be satisfied to guarantee the safety of the final user. For this reason, this work applies a novel criterion to define a failure surface that could prove an invaluable tool in formalizing the embrace of FFF in industry, since part failure prediction can finally be performed. Multiple mechanical tests are executed on coupons developed in a traditional FFF printer, as well as a customized, 6-axis robotic printer necessary to produce specimens in out of ordinary orientations. The results of these tests are used to populate the parameters of the mathematical function that describes the failure envelope. Results indicate strong interaction between axial loads, and a considerable interaction between shear stresses and loads applied in a direction perpendicular to the beads. Interactions between shear stresses and axial loads in the direction of the beads appear negligible.

Keywords: FFF, FDM, Failure Criteria, Off-axis Printing, Mechanical Testing.

Acknowledgments

Thank you Prof. Rudolph and Prof. Osswald for your trust and patience. I couldn't hope for better advisors.

Thank you to Prof. Turng and Prof. Prabhakar for your valuable input and time.

Thank you Tom for your extrusion expertise and your polymer knowledge. The sass was OK too I suppose.

Thank you Luke for building the tools necessary for this whole project to work. That big beard hides a sharp mind -and a lot of patience to answer all my random grammar questions.

Thank you Alec for being an ever-present helping hand, a great classmate, and a good friend. Hope you make ND proud.

Thank you José for putting up with my constant interruptions *en español* from across the desk, and for sharing lab managing duties with me. *Suerte y paciencia para el doctorado.*

Thank you to Thibaut, Colby, Johannes, Peilin, Varun, Ahmed and Brendan. This thesis would look very empty without your contributions!

Thank you to the entire PEC family for creating a great learning environment. I've grown so much with all of you. I hope that you've learned a thing or two with me as well.

Thank you to Ben, Josh, Diego, Iván, Pfeifer, Ian, Abrahan, Maria, Sianna, Conny and Sara for your friendship. Madison was a lot of fun because you were in it.

Gracias a mi familia, a quienes les debo todo.

Gracias a Sonya por tu cariño y paciencia. Que este tiempo que pasamos tan lejos nos traiga en creces momentos juntos. Te amo.

Table of Contents

Front Matter	i
Abstract	i
Acknowledgments	ii
Nomenclature	vi
List of Figures	viii
List of Tables	ix
Introduction	1
1 Background	3
1.1 Additive Manufacturing	3
1.1.1 Advantages, Disadvantages and Success Stories	4
1.2 Fused Filament Fabrication	6
1.2.1 The FFF process	7
1.2.2 Mechanical Properties of FFF parts	9
1.3 Failure Criteria	10
2 A Novel Failure Criterion	12
2.1 The Gol'denblat-Kopnov Model	12
2.2 The Osswald-Osswald Criterion	15
3 Experimental Methods	19
3.1 Material	19
3.2 Sample Preparation	20
3.2.1 Printing Equipment	20
3.2.2 Tensile Specimens	22
3.2.3 Compressive Specimens	23
3.2.4 Torsion and Combined Loading Specimens	24
3.3 Mechanical Testing	26
3.3.1 Tension and Compression Tests	26
3.3.2 Torsion and Combined Loading Tests	27

4 Results	30
4.1 Tensile Tests	30
4.2 Compression Tests	33
4.3 Torsion Tests	34
4.3.1 45° orientation	34
4.3.2 0° and 90° orientation	37
4.4 Combined Loading Tests	39
4.5 Development of the Failure Surface	39
5 Conclusions and Outlook	43
Bibliography	45
A SABIC Cycloc MG94 Datasheet	49
B Failure Surface Code	51
C Failure Surface Data	53
D Surface Plots	55

Symbols and Acronyms

Acronyms

- μ CT Micro Computer Tomography
 ABS Acrylonitrile Butadiene Styrene
 ADT Anderson-Darling Test
 AM Additive Manufacturing
 CAD Computer Aided Design
 EF Extrusion Factor
 FDM Fused Deposition Modeling™
 FFF Fused Filament Fabrication
 GKC Gol'denblat-Kopnov Criterion
 OOC Osswald-Osswald Criterion
 RP Rapid Prototyping
 SLA Stereolithography
 SLS Selective Laser Sintering

Symbols

$\dot{\epsilon}$	Engineering Strain rate	min^{-1}
$\dot{\gamma}$	Shear Strain rate	min^{-1}
ϵ	Engineering Strain	—
γ	Shear Strain	—
μ^{1112}	OOC parameter- slope at pure shear failure in the $\sigma_{11} - \tau_{12}$ plane	—

μ^{2212}	OOC parameter- slope at pure shear failure in the $\sigma_{22} - \tau_{12}$ plane	—
σ	Axial stress	MPa
σ_{11}	Axial stress in the 1-1 direction	MPa
σ_{22}	Axial stress in the 2-2 direction	MPa
σ_{33}	Axial stress in the 3-3 direction	MPa
τ	Shear stress	MPa
τ_{12}	Shear stress in the 1-2 plane	MPa
τ_{13}	Shear stress in the 1-3 plane	MPa
τ_{23}	Shear stress in the 2-3 plane	MPa
S	Shear strength in the 1-2 plane	MPa
S_{45n}	Negative shear strength for 45° specimen	MPa
S_{45p}	Positive shear strength for 45° specimen	MPa
X_c	Compressive strength in the 1-1 direction	MPa
X_t	Tensile strength in the 1-1 direction	MPa
Y_c	Compressive strength in the 2-2 direction	MPa
Y_t	Tensile strength in the 2-2 direction	MPa

List of Figures

1.1	Process flow of AM	3
1.2	Shoes with AM midsoles	6
1.3	The basic FFF machine configuration	7
1.4	Model, toolpath and final part in the FFF process	8
1.5	Typical FFF part mesostructure and its origin	8
1.6	Results from Koch <i>et al.</i> [6]	10
1.7	Comparison of different failure criteria. [23]	11
2.1	Different load directions in an anisotropic material	13
2.2	GKC failure surface developed using data from the WWFE-1 [21]	15
2.3	μ^{2212} parameter in the $\tau_{12} - \sigma_{22}$ plane	16
2.4	λ^{ijjj} parameters in a generic $\sigma_{ii} - \sigma_{jj}$ stress plane	17
2.5	Comparison of GKC and OOC failure envelopes [21]	18
2.6	Failure surface for SLS developed through the OOC [25]	18
3.1	Extrusion line setup	20
3.2	Printing equipment	21
3.3	Print process in <i>Otto</i>	21
3.4	ASTM D-638 Type I coupon (mm)	23
3.5	Toolpath considerations for the tensile coupons	23
3.6	Compression specimen geometry (mm)	24
3.7	Representation of compression samples	24
3.8	S_{45} Torsion specimen geometry (mm)	25
3.9	S_{45} Representation of the 45° specimen	25
3.10	Torsion specimen used for 0° and 90° tests (mm)	26
3.11	Mechanical testing setup	27
3.12	Stress and strain caused by torque on a tubular geometry [25]	28
3.13	Machine setup for combined loading scenarios	29
4.1	Comparison of tensile results.	31
4.2	X_t and Y_t tested samples	31
4.3	ADT results for tensile data	32
4.4	X_c and Y_c tested samples	33

4.5	Comparison of compression results	34
4.6	ADT results for compression tests	35
4.7	Comparison of 45° torsion results	36
4.8	Comparison of 45° torsion results	36
4.9	Comparison of 0° and 90° torsion results	38
4.10	Comparison of tested 0° and 90° torsion specimens	38
4.11	failure envelope in the σ_{11} - σ_{22} plane	40
4.12	failure envelope in the σ_{11} - τ_{12} plane	41
4.13	failure envelope in the σ_{22} - τ_{12} plane	42
4.14	Complete Failure Surface	42

List of Tables

1.1	Advantages and Disadvantages of Additive Manufacturing	5
2.1	Nomenclature of the GKC parameters	14
2.2	Tensorial components of the GKC	14
2.3	Interaction components attainable through the OOC [21]	17
3.1	Mechanical tests required for the OOC	20
3.2	Constant printing parameters	22
4.1	Summary of tensile tests	30
4.2	Summary of compression tests	33
4.3	Summary of 45° torsion tests	37
4.4	Summary of 0° and 90° torsion tests	37
4.5	Summary of combined loading tests	39
4.6	Tensorial components obtained from tests in the σ_{11} - σ_{22} plane	41
4.7	Tensorial components obtained from tests in the σ_{11} - τ_{12} and σ_{22} - τ_{12} planes	41

Introduction

Additive Manufacturing (AM) is an umbrella term that encompasses all fabrication techniques where the final geometry of the part is obtained through superposition of material in a layer-by-layer basis [1]. Developed in the 1980s, this manufacturing technique permits immensely shorter part development cycles, since the transition from a 3D *Computer Aided Design* (CAD) to part fabrication only requires one intermediate step: the use of a slicing engine that converts the geometry of the object into machine instructions [1]. For this reason, AM technologies were initially employed exclusively for prototype development and were referred to as *Rapid Prototyping techniques* (RP). However, recent innovations in the field have caused AM to be considered as a legitimate manufacturing technology since it is also capable of reproducing complex geometries unattainable through traditional methods [1].

While offering great advantages over traditional part fabrication methods, AM comes with its own set of limitations and disadvantages: First and foremost, the use of a stratified build approach tends to produce extremely anisotropic parts. Secondly, the geometric accuracy of the object produced is highly dependent of process parameters, particularly, the thickness of the layers. Finally, as of the time of this writing, AM lacks the standardization and scrutiny that are associated to most traditional manufacturing techniques [1].

Fused Filament Fabrication (FFF), also known under the trademark *Fused Deposition Modeling* (FDM™), represents perhaps the most prevalent AM technique in the market due to the advent of low-cost, desktop 3D printers in the early 2010s [2]. Due to the broad availability of machines and relatively low costs of material, there is a surging interest in optimizing FFF to produce small batches of end-user grade parts. Success stories are varied, but examples include vacuum form molds, fixtures, jigs, and tools used to aid assembly lines in the automotive industry [3, 4, 5]. However, this technology still faces the challenges and limitations that currently affect the field of AM as a whole. Namely, anisotropy introduced through the layer-by-layer build approach makes it difficult to assess the expected mechanical behavior of FFF parts when subjected to important mechanical stresses [2]. For these reasons, multiple attempts have been made to characterize the anisotropy of FFF manufactured objects. Recent studies performed by Koch *et al.* [6] and Rankouhi *et al.* [7] show that the ultimate tensile strength of FFF coupons is sensitive to process parameters such as the layer thickness and, in particular, the orientation in which the plastic strands are laid during

the build process -henceforth referred to as the bead orientation. However, literature related to preventing failure through design is scarce, given the difficulty of using commercially available FFF machines to produce test coupons with unconventional bead orientations, as well as the limitations inherent to commonly used failure criteria that make it difficult to develop an accurate failure surface.

This research applies a novel criterion, tailored for anisotropic materials, to develop a failure surface for FFF parts through mechanical testing of coupons under various types of loading conditions. Certain test specimens were produced using a unique off-axis 3D printer developed in-house that allows production of coupons in unconventional configurations. Such a surface can be an invaluable tool in part design, since catastrophic failure can be prevented in the early stages of part development. This could potentially allow a broader embrace of FFF as a legitimate manufacturing technique in highly demanding engineering fields, such as the aerospace or automotive industries where part failure is to be avoided at all costs.

This work offers a comprehensive overview of AM technologies, FFF and shortcomings of current failure criteria in Chapter 1. Chapter 2 details the failure criterion used throughout this work, as well as outlining its advantages over similar models. Chapters 3 through 4 detail the experimental setup followed, as well as outlining noteworthy results. Finally, conclusions and recommendations are given in Chapter 5 in the hopes of guiding future work on the topic.

1 Background

1.1 Additive Manufacturing

Additive Manufacturing (AM) technologies had their beginnings in the decade of the 1980s. During this time, various independently developed patents were filed across the globe, describing a process that would construct an object by selectively adding layers of material -as opposed to removing excess matter or deforming mass to obtain a desired shape. This represents the core definition of AM: any technology where the final geometry of the manufactured object is obtained through controlled addition of material qualifies as an Additive Manufacturing technique [1].

Advancements in the fields of computing, *Computer Aided Design* (CAD), and controllers, among other technological developments, were necessary to translate the patents into working prototypes, with some eventually becoming the foundations of commercially successful companies -such as 3D Systems in 1986 and Stratasys in 1989 [1, 8, 9]. The basic process of AM has remained largely unchanged from its first iteration in the late 80s: First, a computer model of the object is made using CAD software and exported under the *.stl* file format. Afterwards, the part geometry is stratified, or “sliced”, and translated into machine instructions using a specialized software called *slicing engine*. An AM machine then follows said instructions, commonly referred to as the *toolpath*, to build the object in layers. Finally, the part is available to the user. Depending on either the requirements of the part, or the specifics of the AM technique used, some post-processing may be required [1]. A visual representation of the process is shown in Figure 1.1.

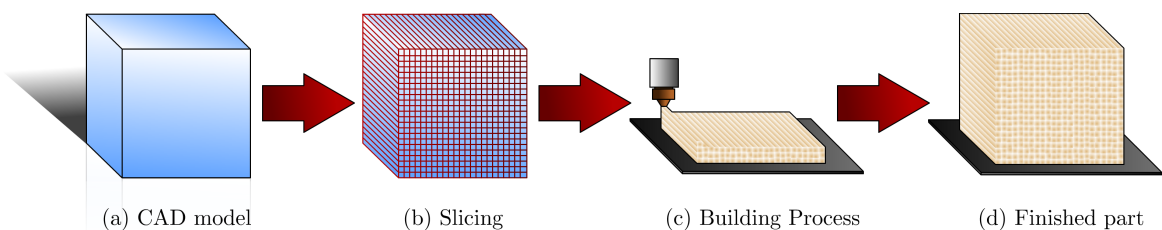


Figure 1.1: Process flow of AM

While all AM technologies operate on the same basic process flow described above, the specifics of each AM technique vary substantially, ranging from processes that use paper and binder, all the way through metal-based, laser tracing technologies. Since this is a rapidly evolving field, no general consensus exists for classifying the multiple AM processes available as of the time of this writing. However, the classification system proposed under the ASTM/ISO 52900 standard [10], has been somewhat accepted by the field and divides AM technologies as follows:

1. **Binder Jetting:** AM techniques where a binding agent is used to selectively promote cohesion in powder materials -generally gypsum, sand or metallic powders [10, 11].
2. **Directed Energy Deposition:** AM processes where a focused thermal energy source (i.e. laser, electron beam, plasma arc) is used to fuse materials as they are being deposited in the build volume. Materials are almost exclusively metals [10, 11].
3. **Material Extrusion:** In this type of AM technology, material is dispensed through a nozzle or orifice. Fused Filament Fabrication belongs to this classification. Materials are almost exclusively thermoplastics [10, 11].
4. **Material Jetting:** AM techniques where build material is deposited selectively in droplets. Materials are usually wax or thermoplastics, but there are examples of metal-based, material jetting techniques [10, 11].
5. **Powder Bed Fusion:** AM processes where portions of a powder bed are selectively fused through application of thermal energy. *Selective Laser Sintering* (SLS) belongs to this category. Materials are usually thermoplastic polymers or metals [10, 11].
6. **Sheet Lamination:** In this type of AM technology, the final part is formed by bonding sheets of material -usually paper or composites [10, 11].
7. **Vat Photopolymerization:** In this AM process, a liquid photopolymer is selectively cured by a light source. *Stereolithography* (SLA), arguably the first AM technology, belongs to this category. Due to the nature of this technique, the only materials used are photopolymers [10, 11].

1.1.1 Advantages, Disadvantages and Success Stories

Since AM processes allow a relatively direct conversion of a CAD model into a constructed object, they were originally exclusively used for prototype development. For this reason, they were initially classified as “*Rapid Prototyping*” (RP) technologies. This terminology is still used today, however, it is being superseded by *Additive Manufacturing* since its potential to become a proper fabrication technique exists [1]. While

being capable of quickly jumping from part design to manufacturing is a great advantage, AM has its own set of drawbacks. Table 1.1 summarizes the most noteworthy set of advantages and disadvantages typical of most AM technologies.

Table 1.1: Advantages and Disadvantages of Additive Manufacturing

Advantages	Disadvantages
Faster product development cycles [1]	Part quality highly dependent on process parameters [1]
No additional tools needed for part fabrication[1]	Stratified build generally results in anisotropic parts [1, 2]
Cost effective for small batches of parts [12, 13, 14]	Costly for production of more than hundreds of parts [12, 13, 14]

Out of all the described advantages and disadvantages, the high anisotropy of AM parts is responsible for the slow embrace of AM in highly demanding engineering fields -such as the aerospace and automotive industries. The highly anisotropic mechanical behavior makes it extremely difficult to predict part failure, therefore, it cannot be implemented in engineering applications where catastrophic failure is to be avoided at all costs. Even so, success stories of implementation of AM in industrial environments are abundant. Below is a number of relatively recent examples:

- **Volkswagen Autoeuropa:** This automotive assembly plant implemented the use of FFF machines to manufacture tools, jigs and fixtures used in their assembly line. They now produce 93% of the tools that were historically externally sourced, and have reportedly cut their tool development time and costs by 95% and 91% respectively [5].
- **General Electric:** GE is currently producing a complex fuel nozzle injector for the LEAP jet engine, using powder based, metal AM. The complex geometry of this component could not be manufactured by any other manufacturing technique. The production plant in Alabama is expected to have 50 AM machines producing 35,000 fuel nozzle injectors annually by 2020 [15].
- **Adidas and New Balance:** Both shoe companies have developed separate approaches to constructing highly optimized, 3D printed midsoles for high performance running sneakers. New Balance makes use of SLS technology to build the intricate geometry of their “*Zante Generate*” sneaker, using powdered TPU elastomer as the parent material. The designed honeycomb structure of the midsole, combined with the flexible material used, is supposed to improve the comfort and support brought by the shoe [16]. Adidas on the other hand chose to develop the “*AlphaEDGE 4D LTD*” running shoe using the CLIP technology by Carbon3D. While the cell geometry in the midsole is also supposed to bring performance and comfort improvements, the final ambition of Adidas is to perfect the technology to a point where a customer can simply go to a shoe store, have their feet

scanned, and receive a fully customized shoe with a 3D printed midsole that fits their particular needs [17, 18]. In both cases, the geometry of the midsole can only be produced by AM. The intricate structures in the midsoles can be seen in Figure 1.2.



(a) New Balance Zante Generate [16]



(b) Adidas AlphaEdge 4D LTD [18]

Figure 1.2: Shoes with AM midsoles

Note that in the cases presented, the main reason behind the usage of AM was either reduction of expenses associated with producing small batches of parts, or the capability of reproducing a unique and complex geometry. This is a trend that is observed in most of the literature describing implementation of AM into industrial scenarios.

While the advantages and disadvantages described here cover the field of AM as a whole, each technique comes with its own set of pros and cons that may make it the preferred method to reproduce a particular product or geometry. This work, however, focuses solely on FFF. The specifics of this process are described in detail in Section 1.2.

1.2 Fused Filament Fabrication

Fused Filament Fabrication (FFF) is an AM technology where the final geometry of the part is obtained through controlled extrusion of a liquid, self-hardening material-usually a thermoplastic polymer in molten state [1]. Originally developed by Stratasys in the 1980s under the still trademarked *Fused Deposition Modeling* (FDMTM) moniker, it has recently become one of the most widely used AM techniques due to the advent of low-cost, desktop FFF machines in the early 2010s caused by the expiration of key patents from Stratasys [1, 2].

1.2.1 The FFF process

At its core, the typical FFF machine consists of a heated build surface commonly referred to as a *build plate*, a specialized tool known as a *printhead*, and the fabrication material -supplied in the form of spools of thermoplastic polymer filament. The printhead is itself composed of a heating element, a nozzle, and some form of driving mechanism that pushes the filament downward. As the thermoplastic material is moved through the heated chamber, polymer melt is formed and extruded through the opening at the tip of the nozzle, producing a *bead*. The molten polymer can then be deposited upon the build plate, where controlled movements of the printhead and the fabrication surface gradually construct the final geometry of the part in a layer-by-layer build approach [1]. The typical setup of an FFF machine can be seen in Figure 1.3. In this example, the printhead moves in the *x-y* plane, while the build plate moves in the *z* direction.



Figure 1.3: The basic FFF machine configuration

Like all AM technologies, the FFF process starts in a computer with a CAD model converted to the *.stl* file format. The geometry is then translated to machine instructions through a *slicing engine*, where the user inputs a plethora of process parameters that include nozzle and build plate temperatures, print speed, layer thickness, and build orientation. Finally the *toolpath* is executed by the FFF printer, building the object in a layer-by-layer basis – sometimes referred to as *2.5D* printing [1, 4]. Figure 1.4 shows an abridged version of the process. The *z* axis indicates the intended build direction. Note how some of the finer details in the original CAD file are lost in the printed part – due in part to the layer height and build orientation selected.



Figure 1.4: Model, toolpath and final part in the FFF process

The process is capable of producing complex geometries that would be otherwise hard to reproduce through other polymer processing techniques, such as injection molding. However, it is bound by the disadvantages described in Section 1.1.1, as well its own unique set of drawbacks. Namely:

- The circular orifice in the nozzle makes FFF incapable of reproducing sharp corners, limits the size of the smallest reproducible feature, and causes the final part to be filled with voids –originating in the junction of round beads. These problems can be seen in Figure 1.5: On the left, a comparison of a 90° corner planned in the toolpath and the final geometry of the printed bead is shown. Note the rounded nature of the turn. On the right, a cross section of an FFF part obtained through *Micro Computer Tomography* (μ CT) shows the voids that form during the printing process.

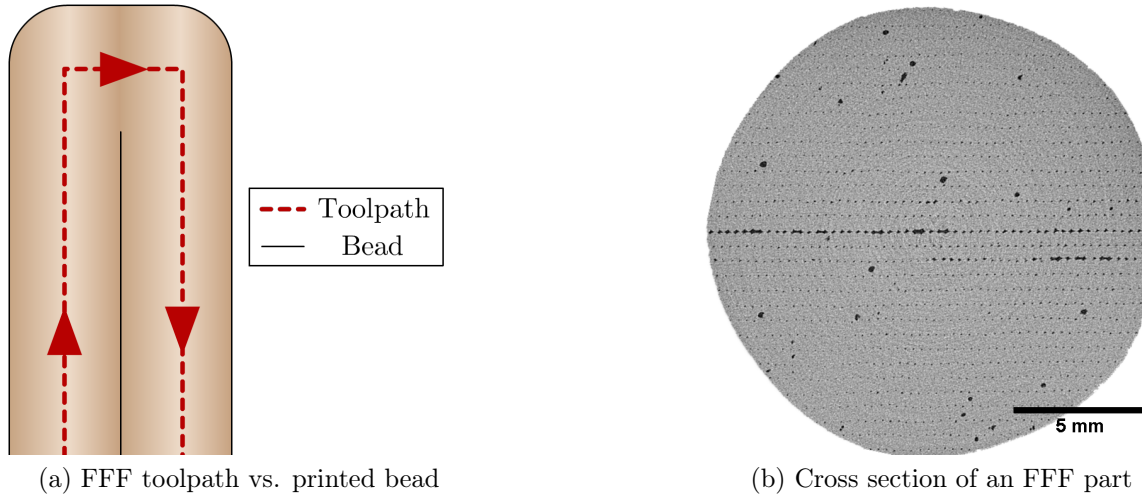


Figure 1.5: Typical FFF part mesostructure and its origin

- The junction of adjacent beads behaves akin to a polymeric weld, and has inferior mechanical properties than the bulk material [2]. This, coupled with the aforementioned voids which can act as stress concentrators, causes FFF parts

to behave in extremely anisotropic manner with diminished mechanical performance when compared to analogous parts obtained through traditional polymer processing technologies – such as injection molding [2].

This last disadvantage is responsible for the slow embrace of FFF as a proper manufacturing technique: the high anisotropy of FFF parts imply that predicting part failure becomes extremely difficult and thus, proper part design that guarantees safe operation of the object under important loads is hard to achieve. For this reason, efforts to characterize the mechanical behavior of FFF parts have existed since as early as the 1990s. Recent examples are presented in Section 1.2.2.

1.2.2 Mechanical Properties of FFF parts

Efforts have been made to characterize the mechanical anisotropy of FFF parts. However, due to the lack of testing standards and problems during toolpath planning, most studies focus solely in the tensile mechanical performance of FFF coupons.

Recent studies performed by Koch *et al.* [6] and Rankouhi *et al.* [7] indicate that the final tensile properties of FFF coupons are particularly sensitive to bead orientation and proper mass output through the nozzle. Other process parameters, such as the layer thickness, have varying degrees of impact upon the final tensile strength of the part. In both studies, tensile coupons were printed with bead orientations of 0° , 45° and 90° in the x - y plane. Results showed that in all the experimental conditions selected, a 0° orientation always behaved closer to the bulk material, whereas a 90° sample always had significantly lower tensile strengths. The 45° samples sat between both extremes. It is important to note that in both studies, toolpath manipulation was necessary to avoid premature failure of the coupons due to stress concentrators originating in void formation due to the elliptical nature of the beads. Figure 1.6 shows some of the results by Koch *et al.* The geometry corresponds to an ASTM Type I Tensile coupon. Injection molded results are denoted *IM* for comparison. Note that the 90° orientation had a tensile strength that was 25% inferior to the IM counterpart, and 20% worse than the 0° oriented FFF coupon. This is a prevalent trend in the consulted bibliography.

Literature for other types of mechanical testing of FFF parts is relatively scarce when compared to tension experiments. Research indicates that the compressive strength of FFF parts tends to be higher than the tensile strength, as well as being less sensitive to process parameters —the bead orientation in particular seems to have a significantly diminished impact upon the compressive strength when compared to its effect upon tensile tests [19, 20]. Shear strength results are virtually non-existent.

Figure 1.6: Results from Koch *et al.* [6]

1.3 Failure Criteria

The increased use of advanced materials in industry has brought upon a necessity to properly characterize their strengths and failure modes. Composites in particular are commonly used in highly demanding engineering fields given that they excel in mechanical properties. However, due to their nature, their behavior is extremely anisotropic. For this reason, it has been of great interest to develop a proper way to model the behavior of anisotropic materials under mechanical stresses as a way to predict part failure – a practice from here on referred to as developing a *failure criterion*.

Early attempts to properly predict failure of anisotropic materials go as far back as 1948 with the Hill model [21]. Further developments led to a plethora of failure criteria, such as the Tsai-Hill, Malmeister, Tsai-Wu, Gol'denblat-Kopnov, Puck, and Cuntze to name a few [21, 22]. A wide variety of criteria exists because a model will rarely capture the complete failure behavior of an anisotropic material. To illustrate this point, refer to Figure 1.7, reproduced from work by Sun *et al.* [23] where a composite glass fiber and epoxy laminate was loaded biaxially, in a direction that was either parallel (σ_{11}), perpendicular (σ_{22}) to the fiber, or a combination of both. Positive stresses indicate tensile load, while negative values point to compressive forces. The data, represented by the white squares, does not agree with any of the used models in the fourth quadrant of the graph. This type of behavior is common throughout the literature: Puck's model is great at predicting shear strengthening effects, but doesn't perform well when dealing with combined axial loading scenarios; the Gol'denblat-Kopnov model by contrast is great at predicting axial stress interactions, but falls short when dealing with shear strengthening effects caused by combined shear-axial loadings. These trends point to the limitations of each model: in order to either facilitate calculations, or due to the difficulty of performing combined loading tests, interaction effects are neglected either

by mathematical choice, or indirectly through the inner workings of the failure criterion [21].

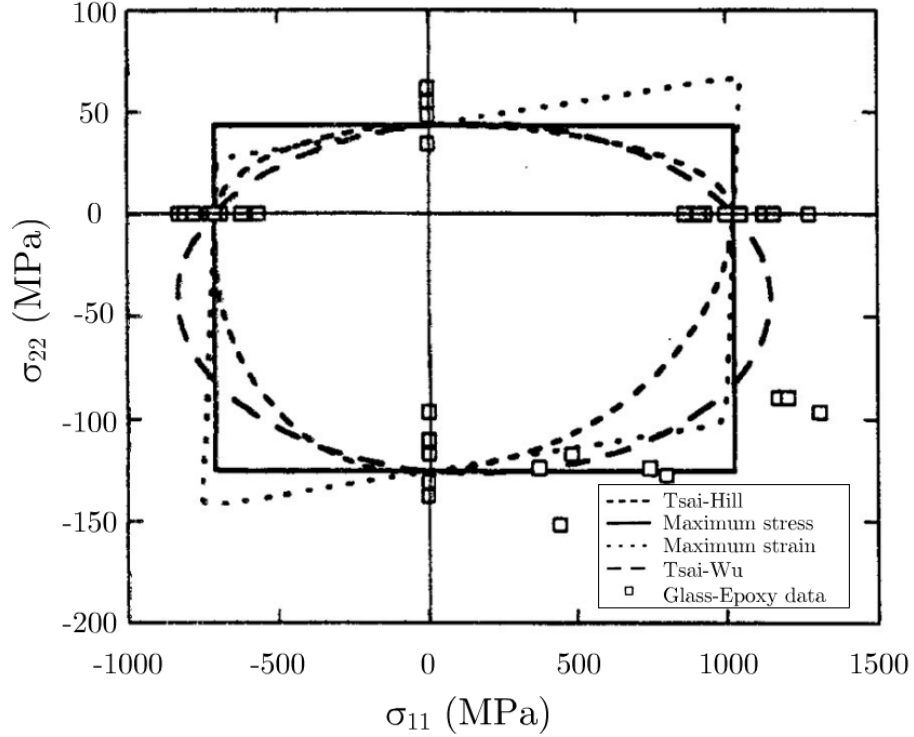


Figure 1.7: Comparison of different failure criteria. [23]

Properly mapping a failure surface through a criterion proves to be an invaluable tool for design, since it allows engineers to assess if a part will perform safely under its intended loading conditions. Such tool could in theory help overcome the main shortcoming of FFF since a properly tailored failure envelope would allow proper part design considerations. However, since no present criterion completely captures the behavior of anisotropic materials, a novel technique is needed. Chapter 2 describes in detail a novel approach, based on the Gol'denblat-Kopnov model, that includes interaction effects to properly describe the failure behavior of anisotropic parts.

2 A Novel Failure Criterion

The Osswald² criterion

As described during Section 1.3 of Chapter 1, currently available failure criteria fail to completely integrate interaction effects into the modeled failure behavior of anisotropic materials. In 2017, Paul and Tim Osswald proposed a model that attempts to overcome these limitations [21]. This recent failure criterion has the following characteristics:

- **Tensor based and purely mathematical:** as opposed to phenomenological or mechanistic models such as the Puck or Cuntze failure criteria.
- **Based on the Gol'denblat-Kopnov model.**
- **Includes stress interactions that other models neglect.**

Originally titled “A Strength Tensor Based Failure Criterion with Stress Interactions”, it will be referred in this work as the Osswald-Osswald Criterion (OOC). This chapter will describe the Gol'denblat-Kopnov model upon which the OOC is based, followed by a proper description of how this novel model implements stress interactions.

2.1 The Gol'denblat-Kopnov Model

The Gol'denblat-Kopnov Criterion (GKC) describes a mathematical function that depends on the stress state of an anisotropic material. Should the computation of this expression exceed a threshold, part failure is to be expected. To that end, a scalar function that depends on stress tensors that completely characterize the state of the material was developed [24]. This function is shown in Equation 2.1, where stresses are denoted σ , and the subindices i,j,k,l denote a particular load direction.

$$f = (F_{ij}\sigma_{ij})^\alpha + (F_{ijkl}\sigma_{ij}\sigma_{kl})^\beta + (F_{ijklmn}\sigma_{ij}\sigma_{kl}\sigma_{mn})^\gamma + \dots \quad (2.1)$$

The terms F_{ij} , F_{ijkl} and F_{ijklmn} represent second, fourth and sixth order tensors respectively. These terms of the equation depend on engineering strength parameters, such as the ultimate tensile and compressive strengths of the material in a particular load direction [21]. Due to the complexity associated with using higher order tensors, Gol'denblat and Kopnov limited their approach to using only the second and fourth order terms. Thus Equation 2.1 is reduced to:

$$f = (F_{ij}\sigma_{ij})^\alpha + (F_{ijkl}\sigma_{ij}\sigma_{kl})^\beta \quad (2.2)$$

In order to attain a linear criterion scalar function, the exponents α and β were assigned values of 1 and $1/2$ respectively. Finally, in plane stress scenarios, the GKC becomes:

$$\begin{aligned} f = F_{11}\sigma_{11} + F_{22}\sigma_{22} + F_{12}\tau_{12} + & (F_{1111}\sigma_{11}^2 + F_{2222}\sigma_{22}^2 + F_{1212}\tau_{12}^2 \\ & + 2F_{1122}\sigma_{11}\sigma_{22} + 2F_{1112}\sigma_{11}\tau_{12} + 2F_{2212}\sigma_{22}\tau_{12})^{1/2} \end{aligned} \quad (2.3)$$

Note that in Equation 2.3 σ and τ denote normal and shear stresses respectively. Figure 2.1 depicts an anisotropic material and all the possible loading directions for reference.

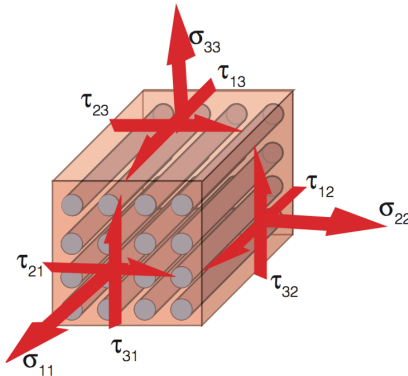


Figure 2.1: Different load directions in an anisotropic material

Per Gol'denblat and Kopnov's design, should the computation of f in Equation 2.3 be greater or equal to 1, part failure is to be expected. However, to simplify calculations, they deliberately assumed the interaction terms F_{1112} and F_{2212} to be zero. This is an important consideration that will come into play when describing the OOC.

Most of the terms in the GKC are obtained through mechanical testing of coupons under pure uniaxial loads in the 1 or 2 direction, or pure shear in the 1-2 plane [21]. In these scenarios, f will be equal to 1 at failure, and the stress state will be known to the user, allowing some of the unknown tensorial parameters to be easily calculated. Using F_{11} and F_{1111} as examples, the process would be as follows:

1. The tensile and compressive strength in the 1-1 direction would be obtained through mechanical testing. These values are named X_t and X_c respectively.
2. Under these failure conditions, Equation 2.3 is reduced to the following system of equations:

$$\begin{cases} +1 = F_{11}X_t + (F_{1111}X_t^2)^{1/2} \\ +1 = -F_{11}X_c + (F_{1111}X_c^2)^{1/2} \end{cases}$$

3. F_{11} and F_{1111} can be obtained, yielding $F_{11} = \frac{1}{2}(\frac{1}{X_t} - \frac{1}{X_c})$ and $F_{1111} = \frac{1}{4}(\frac{1}{X_t} + \frac{1}{X_c})^2$.

The only exception to this procedure would be the F_{1122} component, which requires measuring the positive and negative shear strengths of a coupon with reinforcement oriented in 45° . These parameters are named S_{45p} and S_{45n} respectively. Table 2.1 summarizes the nomenclature used for the strength parameters required to completely populate the failure function of the GKC. Table 2.2 summarizes all the tensorial component calculations.

Table 2.1: Nomenclature of the GKC parameters

Parameter	Description
X_t	Tensile strength in the 1-1 direction
X_c	Compressive strength in the 1-1 direction
Y_t	Tensile strength in the 2-2 direction
Y_c	Compressive strength in the 2-2 direction
S_{45p}	Positive shear strength for 45° specimen
S_{45n}	Negative shear strength for 45° specimen
S	Shear strength in the 1-2 plane

Table 2.2: Tensorial components of the GKC

Component	Formula
F_{11}	$\frac{1}{2}(\frac{1}{X_t} - \frac{1}{X_c})$
F_{1111}	$\frac{1}{4}(\frac{1}{X_t} + \frac{1}{X_c})^2$
F_{22}	$\frac{1}{2}(\frac{1}{Y_t} - \frac{1}{Y_c})$
F_{2222}	$\frac{1}{4}(\frac{1}{Y_t} + \frac{1}{Y_c})^2$
F_{12}	0
F_{1212}	$\frac{1}{S^2}$
F_{1122}	$\frac{1}{8}[(\frac{1}{X_t} + \frac{1}{X_c})^2 + (\frac{1}{Y_t} + \frac{1}{Y_c})^2 - (\frac{1}{S_{45p}} + \frac{1}{S_{45n}})^2]$

2.2 The Osswald-Osswald Criterion

One of the assumptions made in the GKC is that the components F_{1112} and F_{2212} in Equation 2.3 are null. While this simplifies the model, it essentially neglects any interactions between axial loads and shear stresses, namely, the σ_{11} - τ_{12} and σ_{22} - τ_{12} interactions. Practically, this causes the failure surface developed through the GKC to under predict shear strengthening effects exhibited by anisotropic materials loaded in combined axial and shear conditions. Figure 2.2 shows a comparison between experimental data obtained from the first World Wide Failure Exercise (WWFE-I) and the GKC envelope developed for this material. In this example, a unidirectional glass reinforced epoxy composite was tested in multiple loading conditions in the σ_{22} and τ_{12} stress plane. White circles indicate average values for pure uniaxial or shear scenarios. Note how on the first quadrant, the model follows the data closely. However, in the second quadrant, the criterion is relatively conservative, failing to capture the strengthening that occurs when loading the material in compression and shear.



Figure 2.2: GKC failure surface developed using data from the WWFE-1 [21]

The Osswald-Osswald Criterion (OOC) attempts to overcome these limitations by building upon the GKC. For the OOC, the interaction effects are captured through the use of the slopes of the failure surface at any of the points where the engineering strength is known within a particular stress plane [21]. In this failure scenario, the stress state of the coupon is known and easy to implement into Equation 2.3, where $f = 1$. The resulting expression can then be derived with respect to one of the stresses, allowing for the interaction components to be calculated. This is better illustrated through an example. Assuming the component of interest is F_{2212} , the procedure to calculate it through the OOC would be as follows:

1. Obtain all the tensorial components possible through the GKC.
2. Using the $\sigma_{22}-\tau_{12}$ stress plane, take the derivative of Equation 2.3 as a function of σ_{22} in the scenario of failure under pure shear ($f = 1$). This yields the expression:

$$0 = F_{22} + [F_{1212}S(\frac{d\tau_{12}}{d\sigma_{22}}) + F_{2212}S] \quad (2.4)$$

where $\frac{d\tau_{12}}{d\sigma_{22}}$ is the slope of the graph at failure under shear. This term is named μ^{2212} in the OOC and can be obtained by performing combined loading tests. Refer to Figure 2.3 for a visual representation.

3. Rearranging Equation 2.4 to solve for the unknown F_{2212} gives the following expression:

$$F_{2212} = -\frac{F_{22}}{S} - F_{1212}\mu^{2212} \quad (2.5)$$

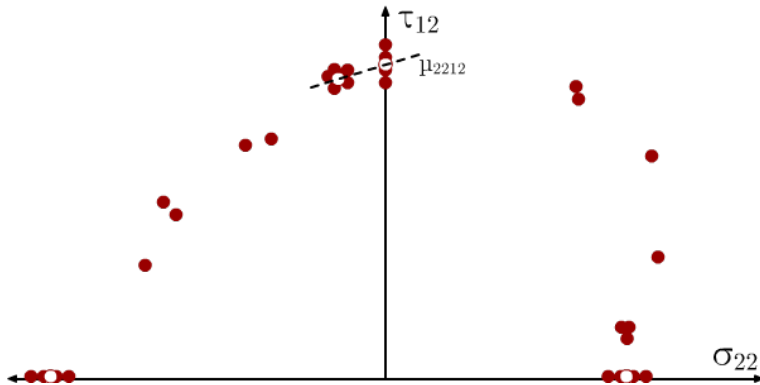


Figure 2.3: μ^{2212} parameter in the τ_{12} - σ_{22} plane

A similar procedure can be followed for any $\sigma_{ii}-\tau_{ij}$ interaction, or even any $\sigma_{ii}-\sigma_{jj}$ components. For this last scenario, the user has four potential choices of slopes to determine the tensorial component of interest. In the OOC, any slope obtained from a $\sigma_{ii}-\sigma_{jj}$ stress plane is named λ^{iijj} , as opposed to μ^{iiji} for slopes in a $\sigma_{ii}-\tau_{ij}$ reference. A schematic of all possible λ^{iijj} is shown in Figure 2.4, while Table 2.3 summarizes all the possible interaction factors available through the OOC, where τ_{ij}^u denotes ultimate shear strength in a particular shear plane.



Figure 2.4: λ^{iijj} parameters in a generic σ_{ii} - σ_{jj} stress plane

Table 2.3: Interaction components attainable through the OOC [21]

Component	Formula
F_{iiji}	$-\frac{F_{ii}}{\tau_{ij}^u} - F_{ijij}\mu^{iiji}$
F_{iiji} through λ_1^{iijj}	$-\frac{(F_{ii} + F_{jj}\lambda_1^{iijj})F_{iiji}^{1/2} + F_{iiji}}{\lambda_1^{iijj}}$
F_{iiji} through λ_2^{iijj}	$-(F_{ii} + F_{jj}\lambda_2^{iijj})F_{jiji}^{1/2} - F_{jiji}\lambda_2^{iijj}$
F_{iiji} through λ_3^{iijj}	$\frac{(F_{ii} + F_{jj}\lambda_3^{iijj})F_{iiji}^{1/2} - F_{iiji}}{\lambda_3^{iijj}}$
F_{iiji} through λ_4^{iijj}	$(F_{ii} + F_{jj}\lambda_4^{iijj})F_{jiji}^{1/2} - F_{jiji}\lambda_4^{iijj}$

Applying the OOC to the data shown in Figure 2.2 demonstrates how the failure surface developed through this new criterion better reflects the failure behavior than its GKC counterpart. A comparison between the two can be seen in Figure 2.5. Note how the OOC envelope captures the shear strengthening better than the GKC.

The OOC offers a way of capturing in a more accurate manner the different failure modes of parts produced through AM technologies. As an example, the model has been successfully implemented by Obst *et al.* in 2018 for SLS manufactured parts produced

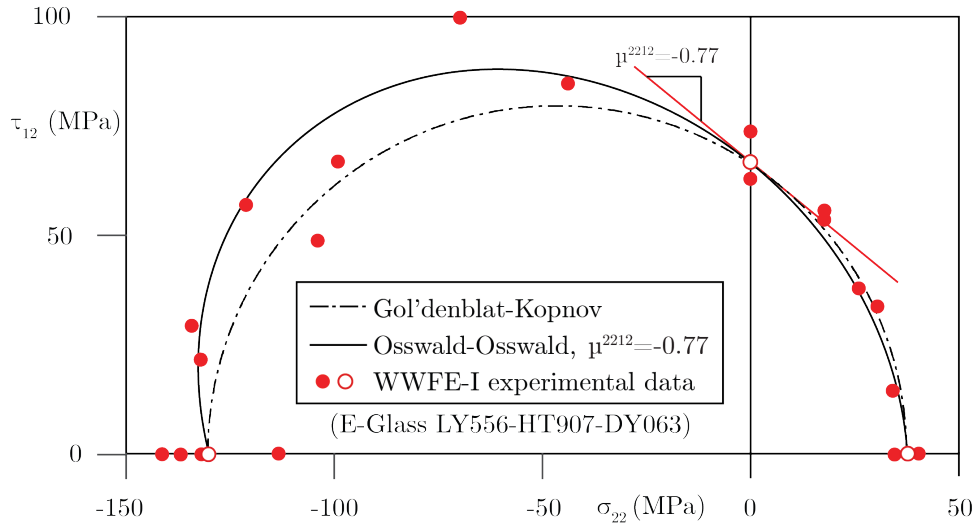


Figure 2.5: Comparison of GKC and OOC failure envelopes [21]

with PA12 [25, 26]. Their results show how the model was able to capture the τ_{12} - σ_{22} and σ_{11} - σ_{22} interactions. The failure surface obtained is shown in Figure 2.6.

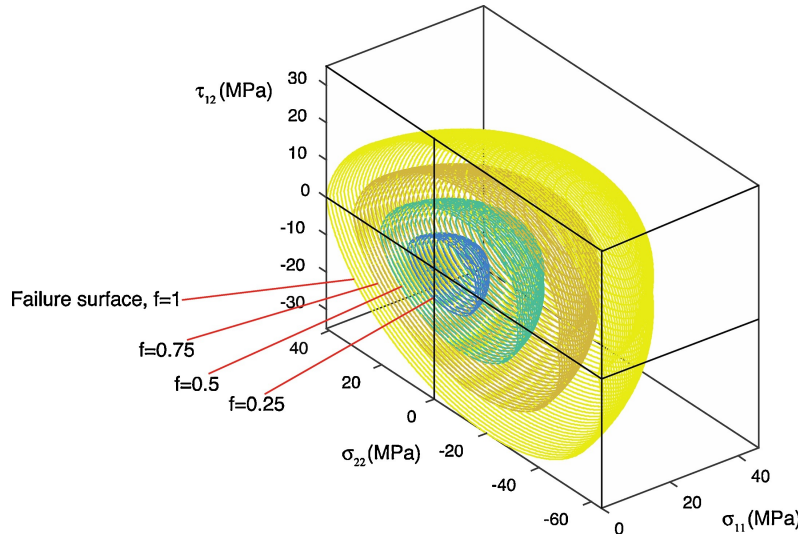


Figure 2.6: Failure surface for SLS developed through the OOC [25]

This work will apply the OOC to FFF, in the hopes that it becomes a tool for safely designing parts intended to be manufactured through this process. Chapter 3 will detail the material and experimental methods used to achieve this goal.

3 Experimental Methods

This chapter explains all the experimental procedures followed to obtain all the parameters necessary to compute the failure surface described by the OOC. This includes detailed information pertaining to the material used, sample geometries and toolpath considerations, as well as describing the equipment used to produce and test the coupons.

3.1 Material

The first step of the experimental work involved development of a custom thermoplastic filament for the FFF process. The reasoning behind this decision was two-fold. First, the use of an off-the-shelf, commercial thermoplastic filament generally does not guarantee that two different spools were produced under the same processing conditions—or even using the same parent material. Secondly, the results from Koch *et al.* [6] show that fluctuations in the filament diameter have an impact in the mechanical properties of FFF parts due to improper volumetric output at the nozzle.

The Cycloc® MG94 material produced by SABIC was chosen for this work. This is an Acrylonitrile Butadiene Styrene (ABS) based material traditionally used for injection molding thin walled parts, as well as extrusion of FFF filament. Refer to the datasheet available in Appendix A for more information. With a reported Melt Flow Index of 11.7 g/10 min, it is an ideal material for both the FFF and extrusion processes [27]. The MG94 was extruded in a setup that consisted of a single screw extruder (Extrudex EDN 45X30D, Germany) with 45 mm screw diameter and L/D ratio of 30D. The hot melt was extruded at 205 °C through a circular die with a 5.8 mm diameter, and then guided through a pre Skinner into a vacuum-assisted, heated water bath (Conair, USA) to cool the extrudate whilst minimizing void formation. The solidified filament was then passed through a 3-axis laser micrometer (LaserLinc, USA) and a belt puller (Conair, USA) configured in a control loop. The dimensions of the filament were controlled by automatically adjusting the speed of the puller if the readings from the micrometer were out of specification—in this case a diameter of 2.85 mm with a tolerance of ± 0.02 mm. Finally, the product was wound onto spools using a filament winder. A schematic of the extrusion setup can be seen in Figure 3.1. Prior to any usage in a printer, the filament was dried in a silo (Novatec, USA) at 82 °C for 3 hours.



Figure 3.1: Extrusion line setup

3.2 Sample Preparation

As explained in Chapter 2, the OOC requires mechanical tests to obtain the multiple tensorial components of the mathematical function that describes part failure. Table 3.1 summarizes the tests required.

Table 3.1: Mechanical tests required for the OOC

Mechanical Test	OOC parameters obtained
Tensile	X_t, Y_t
Compressive	X_c, Y_c
Torsion	S, S_{45p}, S_{45n}
Combined loading	μ^{1112}, μ^{2212}

Given that at the moment of this writing AM testing standards are still in development, custom specimen geometries had to be created in order to test certain loading conditions. Additionally, some bead orientations required are difficult or impossible to reproduce through 2.5-D FFF. Therefore, the use of a customized robotic, off-axis FFF printer was necessary. This section will detail the coupon geometries used to perform all the mechanical tests described in Table 3.1, as well as the printing equipment, and toolpath considerations necessary to properly arrange the printed beads in the desired orientation for each condition.

3.2.1 Printing Equipment

Specimens were produced using either a commercially available desktop FFF printer (Lulzbot TAZ5, USA), or a customized 6-axis robotic printing solution whenever the bead orientation was hard to achieve using a 2.5-D machine. The robotic printer, developed in the Polymer Engineering Center and nicknamed *Otto* [4], was based on a 6-axis robot (ABB IRB-120, Switzerland) and fitted with a stationary printhead mounted on an aluminum frame, chosen to be the same extruder from the traditional printer (LulzBot TAZ Single Extruder Tool Head v2, 0.5 mm nozzle, USA) to minimize machine influence on the results. The printing equipment can be seen in Figure 3.2.

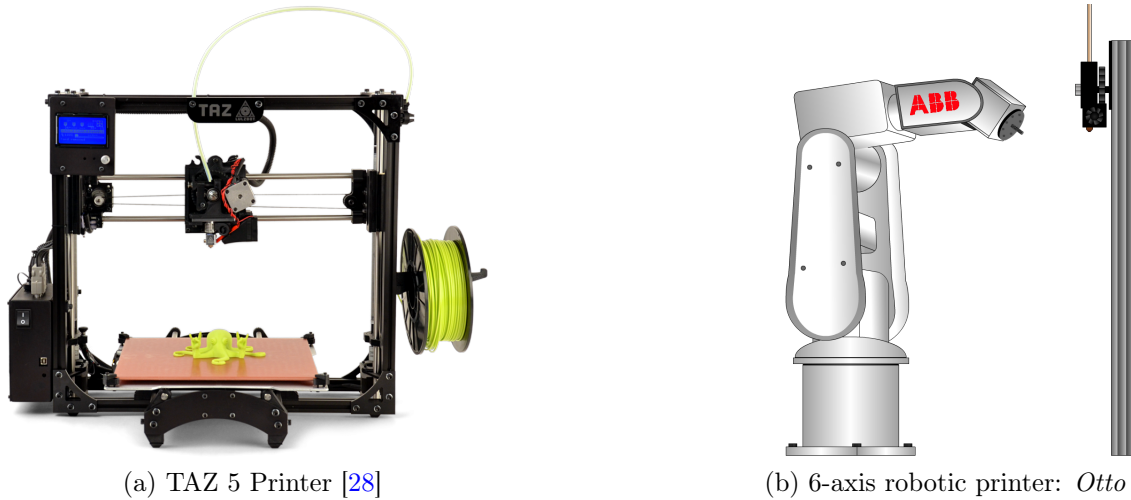


Figure 3.2: Printing equipment

The 6-axis robotic printer’s layout is optimized to produce objects of cylindrical nature. A specialized base plate is attached to the sixth axis of the robot, where a threaded rod allows the attachment of disposable plastic cylinders that act as a build surfaces. A cylindrical core can then be built by *Otto*, upon which beads in any orientation can be deposited after the robot reorients its joints. Refer to Figure 3.3 for a representation of the process. The left side shows the core being produced atop the disposable build surface, followed by the right hand side, where beads are being laid upon the core in a 45° angle.



Figure 3.3: Print process in *Otto*. A core is being printed on the left, while the desired cylindrical geometry with custom bead orientation is being built on the right.

Since printing parameters in FFF are known to impact the mechanical performance of objects manufactured through this technology to varying degrees, a conscious effort was made to keep as many processing parameters as possible constant. Table 3.2 summarizes these values.

Table 3.2: Constant printing parameters

Printing Parameter	Value
Nozzle temperature	220°C
Bed temperature ^a	100°C
Printing Speed	2000 $\frac{mm}{min}$
Layer height	0.2 mm
Path width	0.5 mm
Extrusion Factor	1

Extrusion Factor (EF) refers to a ratio of the area occupied by the cross section of a bead (A_{bead}) divided by the product of the bead width (W_{bead}) with the layer height (H_{layer}). This factor is used to calculate the length of filament (L_{fil}) necessary to produce a bead of known length (L_{bead}) as shown in Equations 3.1 and 3.2. The cross sectional area of the filament (A_{fil}) is known through the filament diameter used by the printer.

$$EF = \frac{A_{bead}}{W_{bead} \times H_{layer}} \quad (3.1)$$

$$\frac{L_{fil}}{L_{bead}} \times A_{fil} = EF \times W_{bead} \times H_{layer} \quad (3.2)$$

3.2.2 Tensile Specimens

Tensile coupons were manufactured on the TAZ5, with bead orientations of 0° and 90° with respect to the load direction in order to test X_t and Y_t respectively. The chosen geometry was the ASTM D-638 Type I coupon [29] which can be seen in Figure 3.4. The toolpath required to produce these samples was developed through *SciSlice*, a customized slicing engine created in the Polymer Engineering Center that allows layer-by-layer and part-by-part controls of crucial process parameters —such as the bead orientation—making it ideal for research in the field of FFF [30].

^aApplicable only to prints performed on the traditional FFF printer.

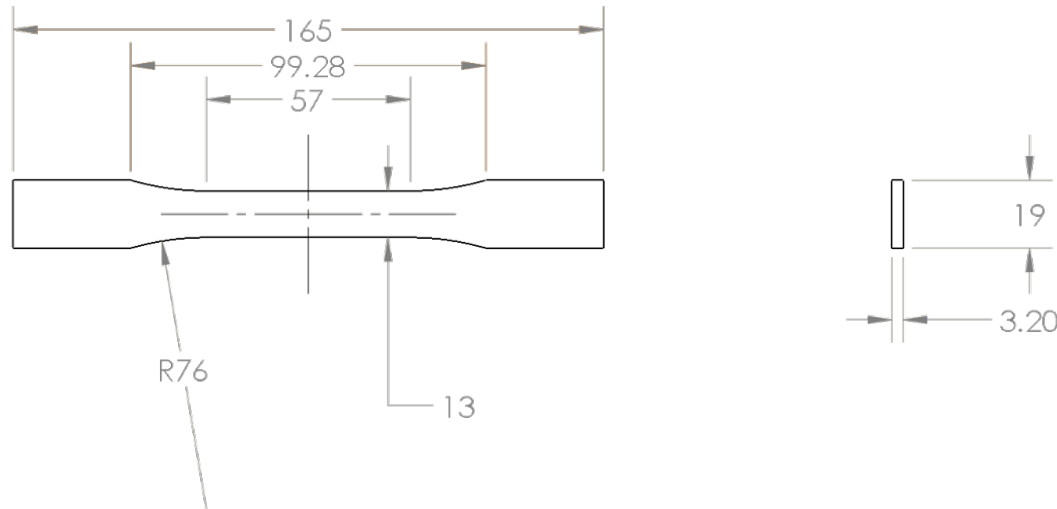


Figure 3.4: ASTM D-638 Type I coupon (mm)

In order to minimize stress concentrators due to printing discontinuities, the 0° specimens were printed using 13 perimeters, also known as *shells*. This produced a continuous toolpath with beads oriented in the loading direction at the neck section of the specimen. No shells were added to the 90° samples. Refer to Figure 3.5 for a visual representation of the coupons.



Figure 3.5: Toolpath considerations for the tensile coupons

3.2.3 Compressive Specimens

Compressive samples were designed with a tubular cross section. This geometry was chosen to mitigate hydrostatic stresses that could artificially increase the compressive strength of the sample if it were made as a completely solid object. Additionally, the cylindrical geometry allowed production of the 0° samples in *Otto*. The geometry can be seen in Figure 3.6.

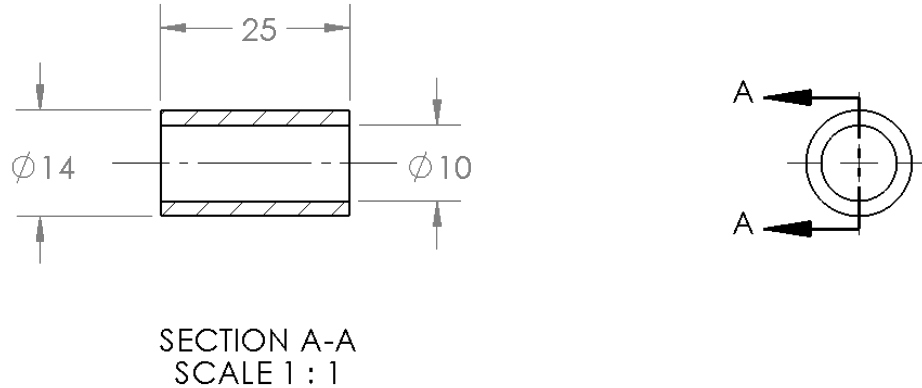


Figure 3.6: Compression specimen geometry (mm)

Compression samples with a bead orientation of 90° with respect to the loading direction were produced using the TAZ5 and *SciSlice*. The coupons with a bead orientation of 0° with respect to the loading direction were made using *Otto* and a customized *Python* script that converted process parameters into instructions for the robotic arm through ABB's *RAPID* toolpathing language. A visual representation of the specimens can be seen in Figure 3.7.

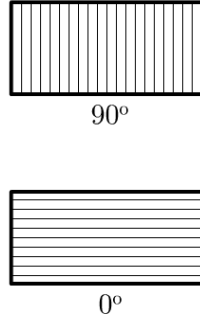


Figure 3.7: Representation of compression samples

3.2.4 Torsion and Combined Loading Specimens

The geometry of the torsion specimens was loosely based in the EN ISO 3167, Type A specimens used by Obst *et al.* [25]. The cross sectional area of the testing area was chosen to be the same as for the compression specimens. This geometry was chosen since its tubular arrangement allows easy integration with the 6-axis robotic printer, as well as offering axisymmetry and reduction of the risk of artificially increasing the strength of the sample due to yielding restrictions associated with using a completely

solid coupon [25]. However, due to toolpathing complications, more than one torsion geometry was necessary. Each one is described in detail below.

45° torsion samples

To test the $\sigma_{11}-\sigma_{22}$ interaction, a torsion sample with beads oriented in 45° was necessary. The geometry, which can be seen in Figure 3.8, consists of a specimen of cylindrical nature, with a filleted, widening change in cross sectional area that culminates in a gripping section. In this portion, three flat surfaces are added to ensure proper contact with the grips of the torsion machine.



Figure 3.8: S_{45} Torsion specimen geometry (mm)

The manufacturing of this type of specimen with *Otto* involved laying 10 layers of beads in a 45° angle atop a cylindrical core of 10 mm in diameter and 95 mm in height. Finally, the gripping section is added using beads in alternating ±45° orientations, culminating in a wider area with a diameter of 24 mm. The flat areas had to be machined in post processing by producing cuts of 1.5 mm in depth in the grips, separated by 120°. A visual representation of the finished sample can be seen in Figure 3.9. Note that the disposable build surface (visible on the left side of the figure) becomes a part of the coupon without impacting the gage section of the sample. All toolpath was generated using a customized *Python* script that converted process parameters into instructions for the robotic arm.

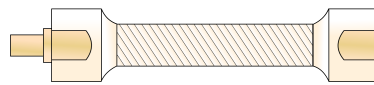


Figure 3.9: S_{45} Representation of the 45° specimen

0° and 90° torsion samples

For the 0° and 90° bead orientations, a specimen redesign was necessary due to tool-pathing problems. Specifically, the length of the 45° torsion specimens proved problematic to print using 0° and 90° bead orientations, each for different reasons. In the case of the 0° orientation, the long and unidirectional travel distance of each bead introduced considerable tool pressure on the core, causing bowing. This was significant enough to cause poor adhesion of the beads towards the end of the specimen. By contrast, production of 90° samples using the original length caused the sixth axis of the robot to heat up considerably and to almost completely maximize its working range.

The torsion specimen was redesigned to have the same cross sectional area as the original 45° torsion samples, but shorter length. An optimal distance was devised through multiple print trials where the length of the specimen was varied between 95 and 50 mm. The chosen geometry is shown below in Figure 3.10. Beads were laid in 0° and 90° orientations using *Otto*, following a similar procedure to the one used to produce the 45° torsion samples.

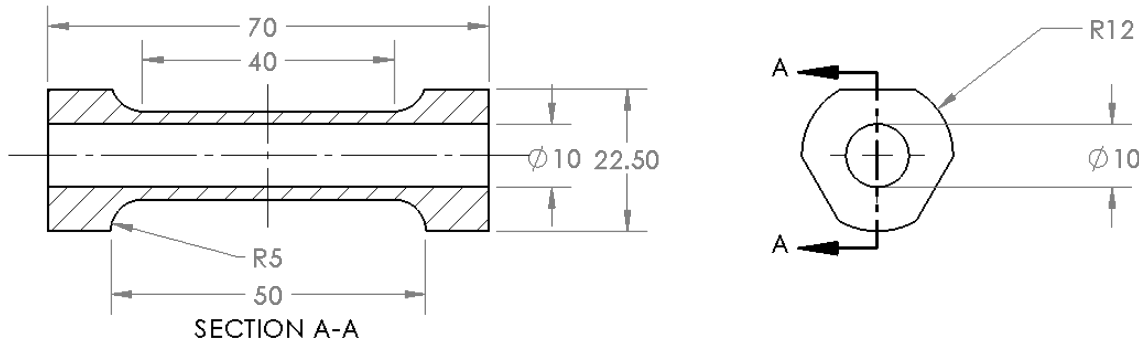


Figure 3.10: Torsion specimen used for 0° and 90° tests (mm)

3.3 Mechanical Testing

3.3.1 Tension and Compression Tests

Tensile and compressive tests were performed with an Instron 5967 dual column universal testing machine, using a 30 kN load cell. All data acquisition was handled through the accompanying Instron Bluehill 3 software. A movement speed of 5 mm/min was used to deform the 50 mm gage section of the tensile specimens, while a testing speed of 2.5 mm/min was used to deform the 25 mm of height of the compression samples. These testing speeds ensured a strain rate of 0.1 min^{-1} across both specimen types.

The tensile specimens were tested using clamp grips and an extensometer. To protect the samples from excessive gripping force, emery cloth tabs were used, as described

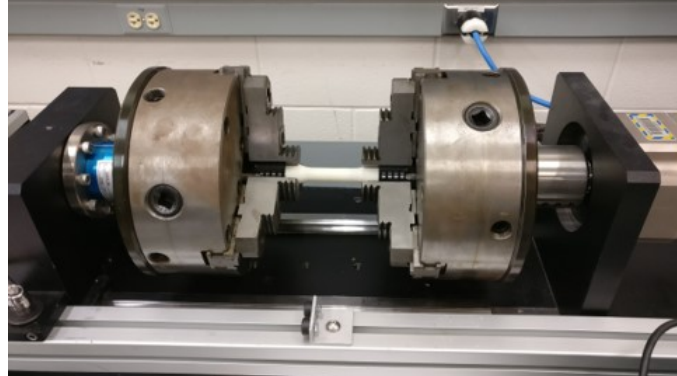
by Mazzei Capote *et al* [2]. Figure 3.11 shows a photograph of the setup. Compressive tests were performed using standard compression platens with the universal testing machine.

3.3.2 Torsion and Combined Loading Tests

All torsion tests were performed using an ADMET eXpert 9618 torsion machine fitted with the MTEST Quattro controller and software suite. The machine sits on a rail system that allows the sample to deform freely during testing. The equipment has two adjustable jaws, with three contact surfaces that holds the sample in place, as shown in Figure 3.11. Of the two jaws, one rotates as controlled by a servomotor, while the other is fixed in terms of angular movement.



(a) Tensile setup



(b) Torsion setup

Figure 3.11: Mechanical testing setup

A conscious effort was made to maintain the same strain rate of 0.1 min^{-1} used for the tensile and compression tests. The approach used was the same described by Obst *et al.* [25]. The initial assumption is that the shear strain rate ($\dot{\gamma}$) is twice the engineering strain rate ($\dot{\epsilon}$), as shown in Equation 3.3.

$$\dot{\gamma} = 2 \times \dot{\epsilon} \quad (3.3)$$

Figure 3.12 represents a tubular element of outer radius ρ and length L , subjected to a torque T . Using this image as reference, one can see that if point B is fixed in space —as is the case of the stationary jaw of the torsion machine used throughout this work—point A will deform to position A'. The angle of twist Φ can then be approximated using the arc length AA' as $AA' = \rho \times \Phi$ for small values of shear strain γ . It can also be seen in Figure 3.12 that the relationship $AA' = L \times \gamma$ also exists. From this, Equation 3.4 can be obtained.

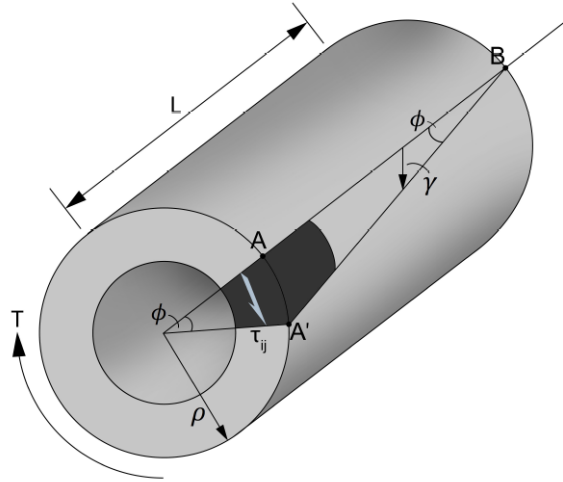


Figure 3.12: Stress and strain caused by torque on a tubular geometry [25]

$$L \times \gamma = \rho \times \Phi \quad (3.4)$$

Finally, after rearranging and deriving with respect to time, Equation 3.5 is obtained.

$$\dot{\Phi} = \frac{L \times \dot{\gamma}}{\rho} \quad (3.5)$$

For this work, $\dot{\gamma}$ is known to be $2 \times 0.1 \text{ min}^{-1} = 0.2 \text{ min}^{-1}$, as dictated by Equation 3.3 and the testing conditions chosen for the tensile and compressive tests. In the case of the 45° specimens, preliminary tests performed in positive torsion showed an average outer radius of 6.91 mm and a mean length of failure propagation of 54 mm. Using these values in Equation 3.5 yields a rotational speed of 1.56 rad/min, or $89.4^\circ/\text{min}$. Following a similar procedure for the 0° and 90° samples, the angular speed of the torsion test was calculated, using L as 40 mm, to be $63.7^\circ/\text{min}$.

In the case of combined loading scenarios, the setup was fitted with a pulley system that allowed a weight to pull the sample in a nominal direction, while the torsion machine applied shear stresses. Refer to Figure 3.13 for a visual representation of the compressive and tensile force setup of the torsion machine.

The shear stress from the torsion tests was obtained through Equation 3.6, where τ_{ij} , R , T , and J_z represent the shear stress in the ij plane, the outer radius of the test section of the sample, the torque applied, and the second moment of area respectively.

$$\tau_{ij} = \frac{T \times R}{J_z} \quad (3.6)$$

For this case, the second moment of area is defined as described in Equation 3.7, where r represents the inner radius of the tubular specimen.

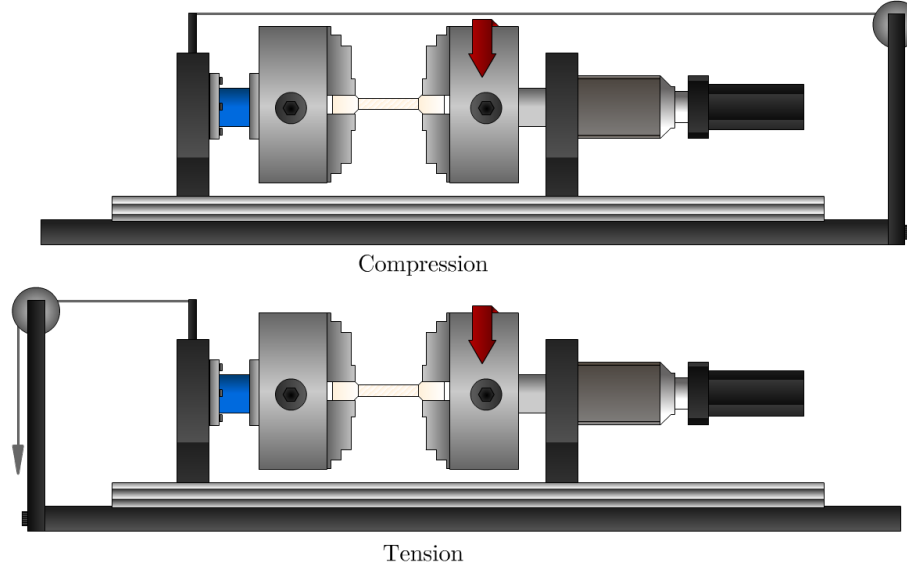


Figure 3.13: Machine setup for combined loading scenarios

$$J_z = \frac{\pi \times (R^4 - r^4)}{2} \quad (3.7)$$

Finally, combining Equations 3.6 and 3.7 yields Equation 3.8

$$\tau_{ij} = \frac{2 \times T \times R}{\pi \times (R^4 - r^4)} \quad (3.8)$$

Chapter 4 will discuss in detail all results that stem from the experimental methods described. Finally, the failure envelope will be calculated using the mathematical relations described in Chapter 2.

4 Results

This chapter presents all the results originating from the experimental procedures described in Chapter 3. Additionally, details are provided regarding data processing, and the calculations that lead to the definition of the desired failure surface.

4.1 Tensile Tests

Performing tensile tests showed that the values of X_t and Y_t were significantly different, in accordance to the literature review presented in Section 1.2.2. An initial number of 20 samples per orientation was produced, however, multiple specimens failed outside the gage section of the coupon and thus, data originating from these coupons was considered invalid and promptly discarded. The valid results are summarized in Table 4.1. Note that X_t was on average 9.16 MPa higher than Y_t , a difference of 22.7%.

Table 4.1: Summary of tensile tests

Information	X_t	Y_t
Average [MPa]	40.29	31.13
Standard Deviation	0.75	0.58
Number of samples	19	12
Lowest measurement [MPa]	39.37	29.68
Highest measurement [MPa]	40.90	32.08

The behavior of both sets of samples was completely different. Coupons used to measure X_t clearly showed whitening of the gage section, indicating plastic deformation. Specimens used for Y_t on the other hand generally failed between beads and rarely showed any change in color. Figure 4.1 clearly shows the difference in mechanical behavior. Note how the X_t specimen shows a ductile failure, as opposed to brittle breakage for the Y_t sample. Figure 4.2 shows both tested samples side by side.

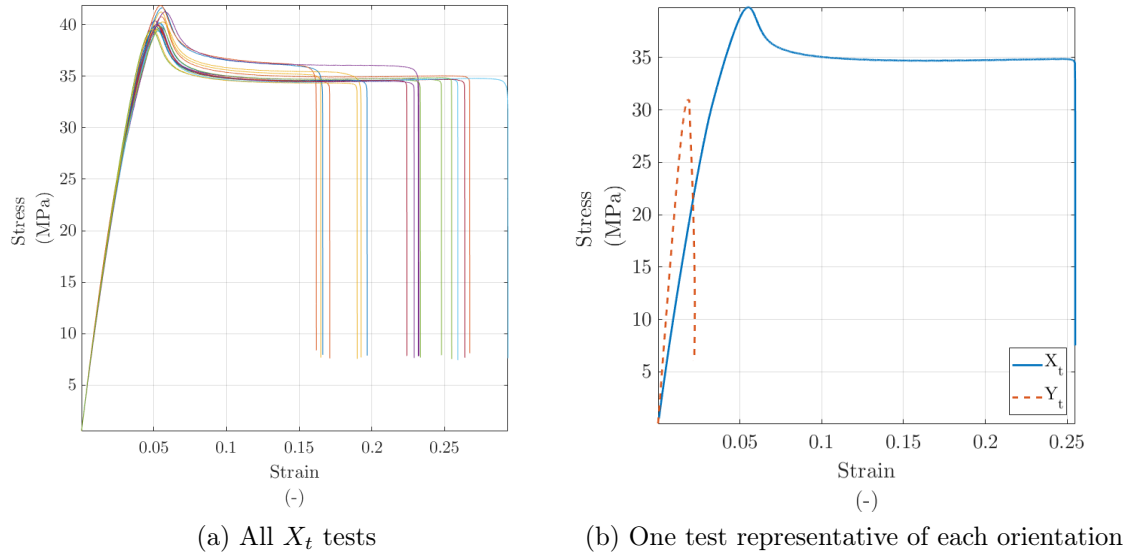


Figure 4.1: Comparison of tensile results.

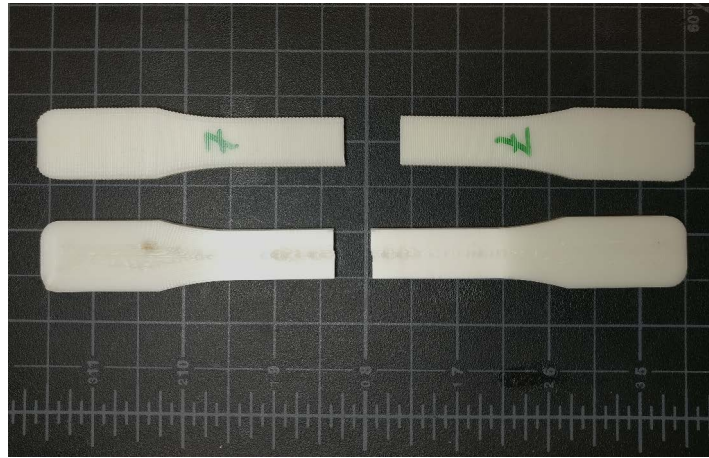


Figure 4.2: Y_t (top) and X_t (bottom) tested samples. Scale in inches. Note whitening in gage section for X_t specimen.

Anderson-Darling tests (ADT) were performed on the results to validate if the data follows a normalized distribution. In the case of X_t , the ADT yields a p-value of 0.023. Thus, on a 95% confidence interval, a normalized distribution can be discarded. This can be seen graphically in the goodness of fit plot, where data points fail to align with the slope that corresponds to a theoretical Gaussian distribution. By contrast, performing the ADT on the Y_t samples fails to reject a normalized distribution using the same confidence interval, offering a p-value of 0.109. The results from ADT can be seen in Figure 4.3.

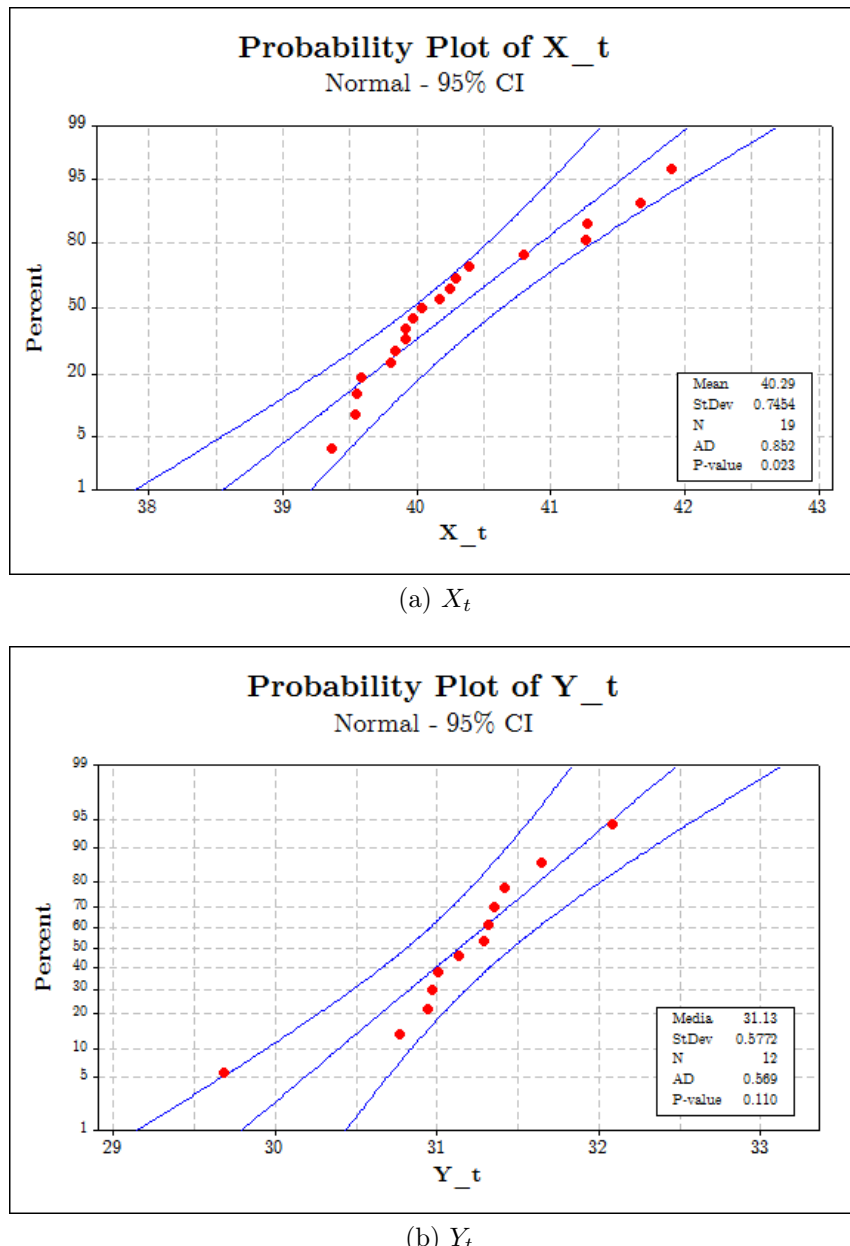


Figure 4.3: ADT results for tensile data

4.2 Compression Tests

For the compression tests, a total of 25 samples were produced for each orientation. However, a number of coupons were discarded due to manufacturing defects. Table 4.2 summarizes the test results.

Table 4.2: Summary of compression tests

Information	X_c	Y_c
Average [MPa]	43.91	57.96
Standard Deviation	3.23	1.81
Number of samples	25	21
Lowest measurement [MPa]	37.95	54.93
Highest measurement [MPa]	48.87	61.39

Surprisingly, both sets of specimens had different failure behavior. The Y_c samples displayed pure ductile behavior through testing. A clear maximum stress can be observed at the yield point in a stress-strain graph, and all samples showed localized whitening and deformation along the center of the specimen. By contrast, the X_c samples showed a considerably lower yield point, cracking sounds were common during testing, and specimens deformed in a way that formed petal-like structures due to contiguous bead delamination. Figure 4.4 shows X_c and Y_c samples side by side post testing, where the different failure behavior becomes evident.



Figure 4.4: X_c (left) and Y_c (right) tested samples. Scale in inches. Note petal-like structure of X_c sample.

The difference in mechanical behavior can be seen clearly in Figure 4.5, where stress-strain curves for X_c and Y_c are compared. Note the erratic behavior of the X_c sample, caused by delamination of adjacent beads.

Performing ADT on the data reveals a p-value of 0.072 for Y_c , and 0.056 for X_c , thus, normalized distributions cannot be discarded on a 95% confidence interval. These tests can be seen in Figure 4.6.

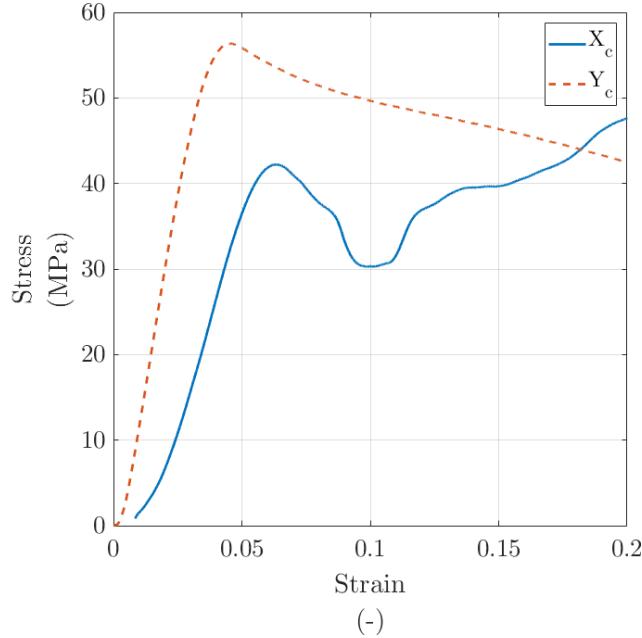


Figure 4.5: Comparison of compression results. One test representative of each orientation shown.

4.3 Torsion Tests

4.3.1 45° orientation

A total of 30 samples were produced with a 45° bead orientation, divided evenly for tests in positive and negative shear. As was the case for tensile and compressive tests, a number of specimens had to be discarded due to undesired behavior during testing. A common problem was delamination of the grips, thus requiring the data to be discarded.

Results showed significant difference in behavior depending on the direction of the applied torque. The S_{45p} samples showed a completely brittle behavior, with fracture occurring between beads, as opposed to ductile failure in the center of the specimen for the S_{45n} coupons. This resulted in an average difference of roughly 17 MPa between both sets of data. Results are summarized in Table 4.3 and a graph comparing the behavior of both sets of samples can be seen in Figure 4.7. Note how the positive shear sample fails at low angles in a completely brittle manner. An ADT reveals p-values of 0.841 and 0.133 for the positive and negative shear tests respectively. This implies that normalized distributions can't be discarded on a 95% confidence interval.

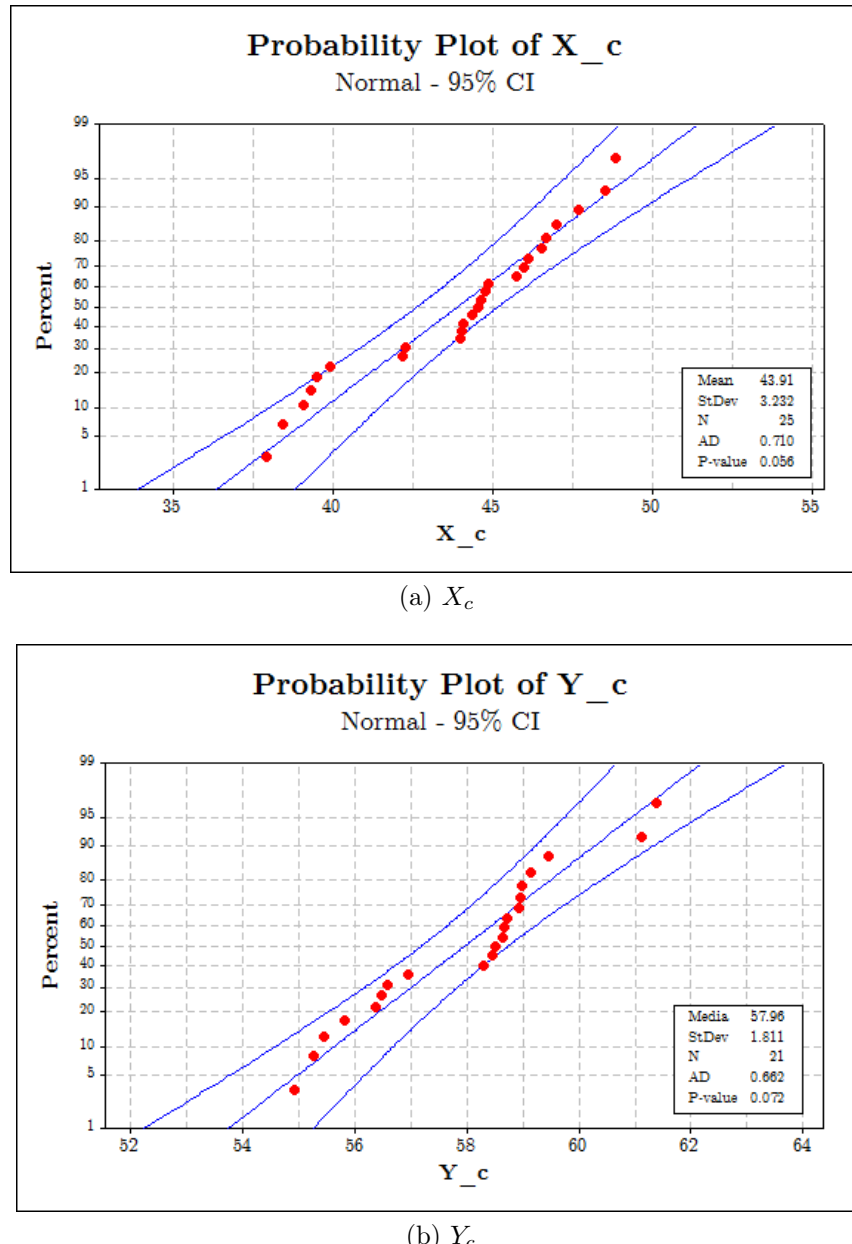


Figure 4.6: ADT results for compression tests

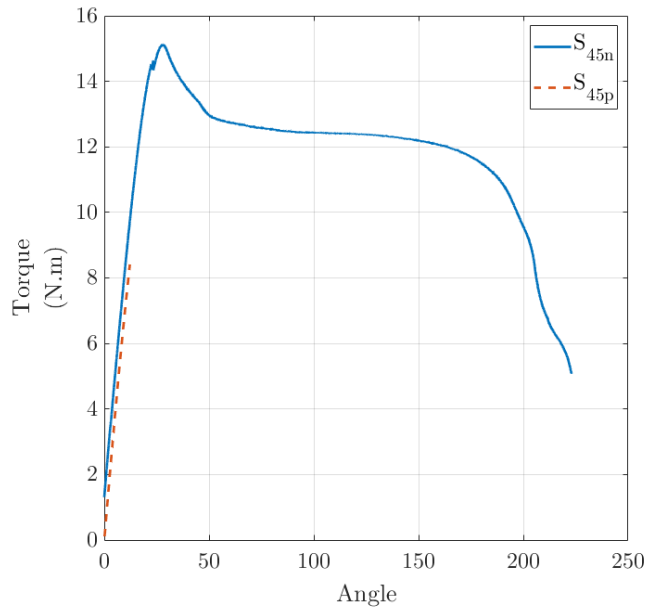


Figure 4.7: Comparison of 45° torsion results. One test representative of each shear direction shown.

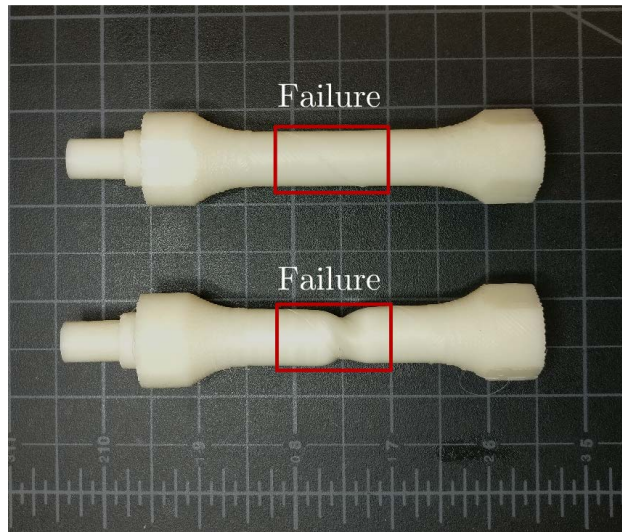


Figure 4.8: Comparison of 45° torsion samples. Positive shear (top) caused bead delamination and brittle failure, whereas negative shear (bottom) produced plastic deformation of the gage section

Table 4.3: Summary of 45° torsion tests

Information	S_{45p}	S_{45n}
Average [MPa]	20.80	38.17
Standard Deviation	2.50	0.71
Number of samples	9	9
Lowest measurement [MPa]	17.21	37.39
Highest measurement [MPa]	24.61	39.62

4.3.2 0° and 90° orientation

A total of 10 samples were produced for each orientation, however, two were discarded for the 0° raster due to manufacturing defects. Table 4.4 summarizes the results from the torsion tests. These were used in conjunction with combined loading data to determine shear and axial stress interactions, as well as the maximum shear strength in the 1 – 2 plane.

Table 4.4: Summary of 0° and 90° torsion tests

Information	S_0	S_{90}
Average [MPa]	23.35	23.41
Standard Deviation	2.78	3.21
Number of samples	8	10
Lowest measurement [MPa]	18.52	18.27
Highest measurement [MPa]	26.56	26.60

It can be seen that both orientations produced nearly identical shear stress results. In both cases, samples behaved in an extremely brittle manner, delaminating along contiguous beads. In the case of the 90° orientation, this usually resulted in complete breakage of the specimen. This can be appreciated in Figure 4.9, where failure is abrupt and violent in a Torque-Angle graph, as well as in Figure 4.10, where tested specimens for both orientations can be seen. Since, practically speaking, both orientations produced the same maximum shear strength result, S_0 will be used for further calculations as the parameter S described in Table 3.1. Performing ADTs on both sets of data reveals p-values of 0.577 and 0.066 for S_0 and S_{90} respectively, thus, normalized distributions cannot be discarded in a 95% confidence interval. The extremely brittle behavior of the samples caused results to have a considerable spread.

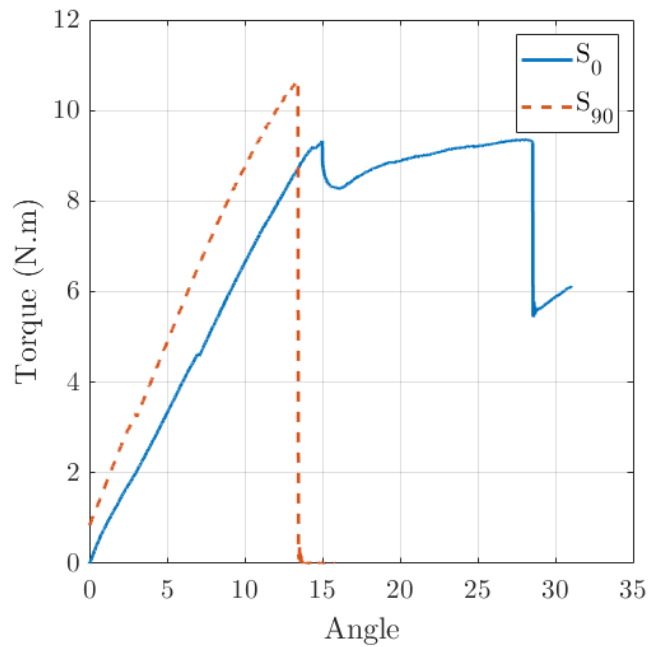


Figure 4.9: Comparison of 0° and 90° torsion results. One test representative of each orientation shown.

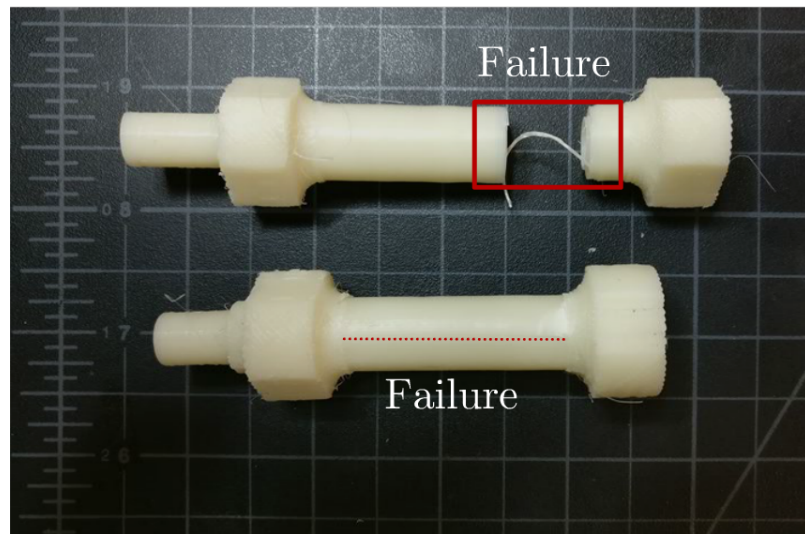


Figure 4.10: Comparison of tested 0° and 90° torsion specimens. 90° coupons (top) generally separated in parts, whereas 0° specimens (bottom) would delaminate along beads, as highlighted by the red dotted line. Scale in inches

4.4 Combined Loading Tests

Combined loading scenarios involved testing 10 samples in shear and tension, and 10 in shear and compression, totaling 20 samples for each orientation. These results were plotted in the $\tau_{12} - \sigma_{11}$ and $\tau_{12} - \sigma_{22}$ planes to develop the terms μ_{1112} and μ_{2212} respectively. Once again, a number of samples was discarded due to manufacturing defects or unwanted failure during testing. A summary of the results can be seen in Table 4.5. Here the superscripts t and c indicate tensile and compressive axial loads respectively, whereas the subscript denotes the orientation of the beads in the torsion specimen. The axial stress was on average 5.8 MPa, attained by hanging a 14.8 kg mass on the setup described in Figure 3.13. All samples failed in identical manner to that described in pure shear scenarios. A slight decrease in shear strength can be appreciated for the S_{90}^t scenario.

Table 4.5: Summary of combined loading tests

Information	S_0^t	S_0^c	S_{90}^t	S_{90}^c
Average [MPa]	23.38	23.13	20.80	22.62
Standard Deviation	2.23	2.98	2.33	2.36
Number of samples	8	10	10	9
Lowest measurement [MPa]	19.03	18.15	16.37	18.57
Highest measurement [MPa]	26.46	26.28	23.93	26.50

4.5 Development of the Failure Surface

The failure surface calculations were performed using MATLAB® code based on previous work by Obst *et al.* [25] and the mathematical relations shown in Chapter 2. This code can be found in Appendix B for reference. Appendices C and D include MATLAB® code that recreates the data and envelopes shown here.

Calculations were based on the average values obtained from the mechanical tests in order to incorporate a probabilistic approach as developed by Zaitsev, Pashkov and Strelyaeve [31]. In practice, this signifies that the condition $f = 1$ in Equation 2.3 is equivalent to a probability of part failure equal to 50%.

Starting with the $\sigma_{11}-\sigma_{22}$ plane, it can be seen that the failure envelope has a slight tilt, agreeing with the difference observed between compressive and tensile strengths in both directions, as well as the difference in behavior for the S_{45} tests. Refer to Figure 4.11 for a graph showing the calculated failure envelope, including the experimental data for reference.

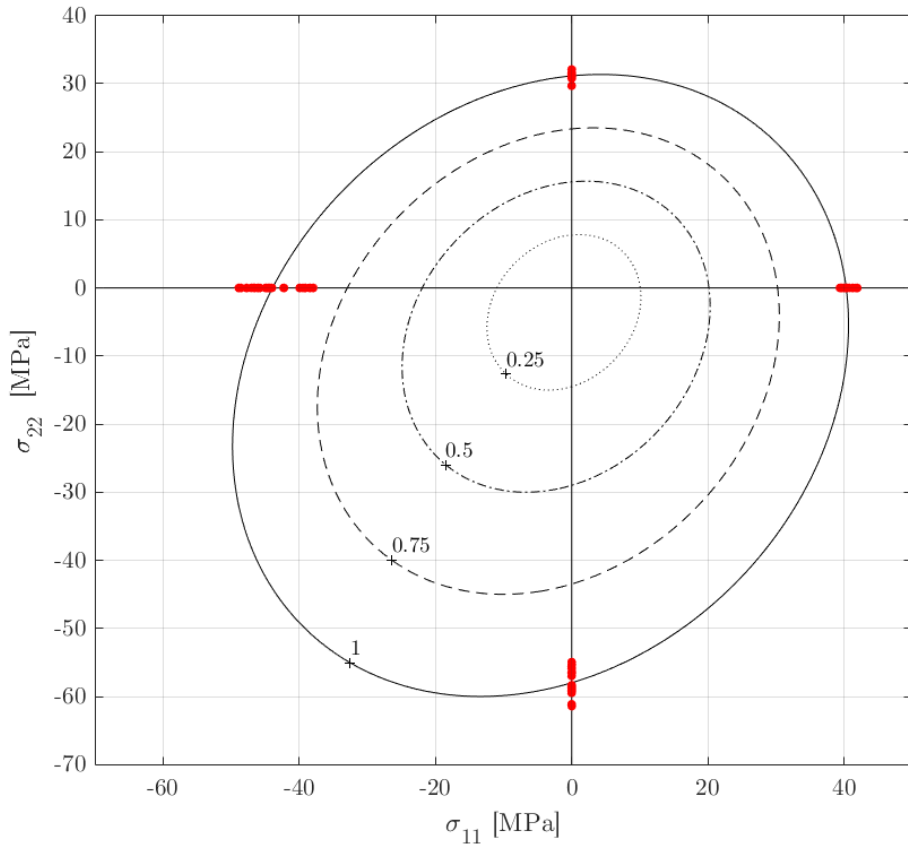


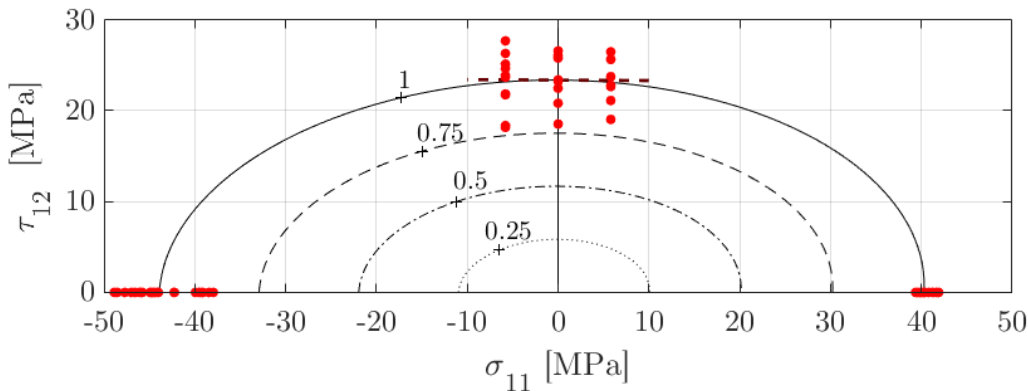
Figure 4.11: σ_{11} - σ_{22} plane including data of X_t , X_c , Y_t and Y_c tests. Graph shows calculated f values of 1, 0.75, 0.50 and 0.25 to illustrate safety factors of 1, $4/3$, 2 and 4 respectively.

It can be seen from the tilt of the envelope that there is an interaction between the transverse and longitudinal stresses. Figure 4.11 indicates that FFF parts produced with the print parameters used should show strengthening when loaded bi-axially in compression. Further experimental work would be of interest to compare bi-axial compression test data to this result. Computing all tensorial components associated with the σ_{11} - σ_{22} plane results in Table 4.6. Note how F_{1122} is negative and in the same order of magnitude as F_{1111} and F_{2222} .

Using the results from combined loading tests plotted in the 11 – 12 and 22 – 12 planes allows the calculation of the slopes μ^{1112} and μ^{2212} . Beginning with the 11 – 12 plane, it can be seen that the averages for S_0 , S_0^c and S_0^t were extremely close to each other, and the spread of the data occludes any trends. Using the averages for S_0 and S_0^t to calculate the slope yields μ^{1112} equal to 5.2×10^{-3} , a value that's practically zero. Using this parameter, the failure surface shown in Figure 4.12 can be obtained. A dashed line representing μ^{1112} is added for reference.

Table 4.6: Tensorial components obtained from tests in the σ_{11} - σ_{22} plane

Component	Value
F_{11}	1.023×10^{-3}
F_{1111}	5.663×10^{-4}
F_{22}	7.435×10^{-3}
F_{2222}	6.095×10^{-4}
F_{1122}	-1.017×10^{-4}

Figure 4.12: σ_{11} - τ_{12} plane including data of X_t , X_c , S_0 , S_0^t and S_0^c tests. Graph shows calculated f values of 1, 0.75, 0.50 and 0.25 to illustrate safety factors of 1, $4/3$, 2 and 4 respectively.

The 22 – 12 plane by comparison reveals a slight interaction. It can be seen through the use of combined loads that there is a slight decrease in the shear strength of the specimens when a tensile load is applied in the 2 – 2 direction. A slope of -0.2 was chosen for μ^{2212} . Figure 4.13 shows the resulting surface with the data and a line with a slope of -0.2 overlaid for reference.

Finally, using the chosen values of μ^{1112} and μ^{2212} , the remaining parameters of the failure surface can be calculated. These are available in Table 4.7. These values were then used to plot the complete failure surface shown in 4.14.

Table 4.7: Tensorial components obtained from tests in the σ_{11} - τ_{12} and σ_{22} - τ_{12} planes

Component	Value
F_{12}	0
F_{1212}	1.834×10^{-3}
F_{1112}	-3.428×10^{-5}
F_{2212}	4.841×10^{-5}

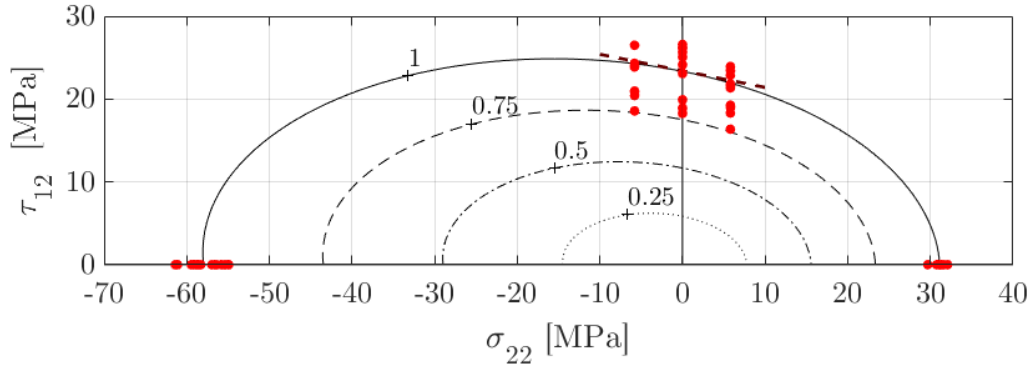


Figure 4.13: σ_{22} - τ_{12} plane including data of Y_t , Y_c , S_{90} , S_{90}^t and S_{90}^c tests. Graph shows calculated f values of 1, 0.75, 0.50 and 0.25 to illustrate safety factors of 1, $4/3$, 2 and 4 respectively.

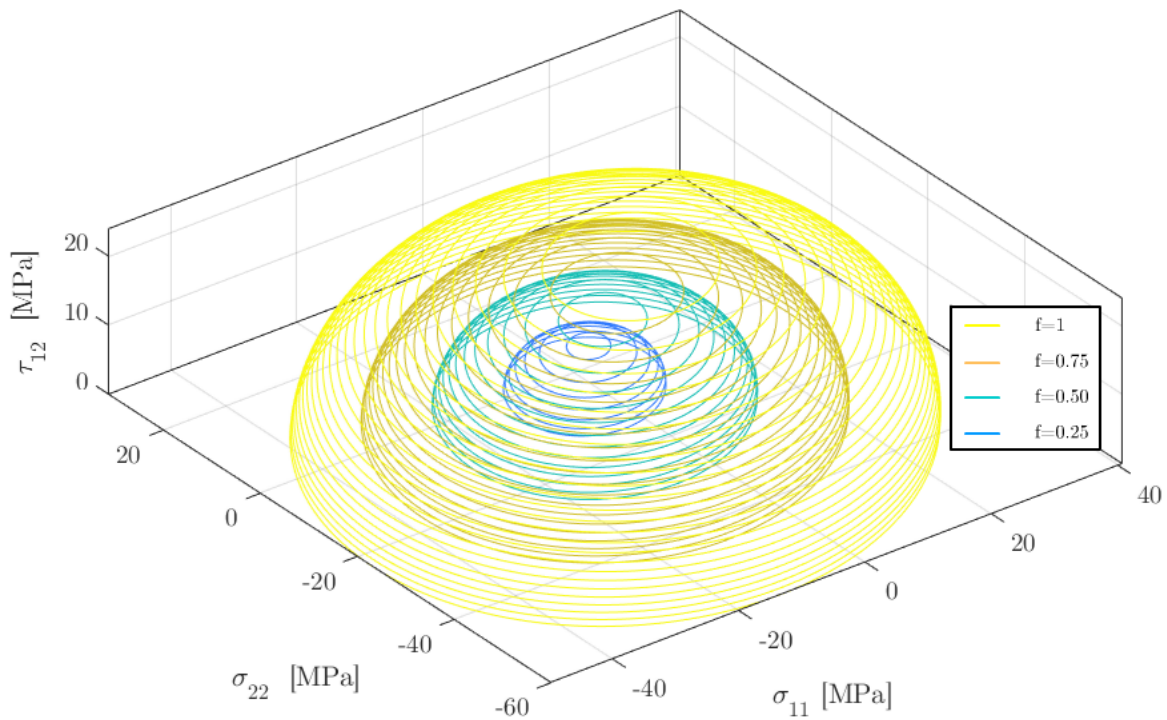


Figure 4.14: Complete Failure Surface plotted with calculated f values of 1, 0.75, 0.50 and 0.25 to illustrate safety factors of 1, $4/3$, 2 and 4 respectively.

5 Conclusions and Outlook

The acceptance of FFF as a formal manufacturing technique still has to overcome a plethora of issues and standardizations, including the ability to predict part failure. This work proves that applying the Osswald-Osswald failure criterion to FFF is not only possible, but can potentially serve as a tool towards achieving part failure prediction. This research also reveals a series of interesting points regarding the mechanical properties of FFF parts. First and foremost, results indicate that there is a strong interaction between axial loads, resulting in a considerable strengthening effect in bi-axial compression scenarios. The model also captures a slight interaction between shear and axial stresses in the direction perpendicular to the beads. Surprisingly, the interaction between shear and axial stresses in the direction of raster seems negligible. This knowledge proves invaluable when designing FFF parts that will serve in an application that implies being subjected to important loads. However, much work could still be done in order to further build upon the concepts and results presented in this work. Below are some suggestions regarding future venues, presented in no particular order of importance.

- **Develop a search algorithm for optimal interaction slopes:** At the moment, the optimal interaction slope is found through trial and error, and visual inspection of the data by the user of the OOC. The criterion could benefit from an algorithm that applies optimization techniques to find the best slope automatically and through mathematically sound and repeatable methods.
- **Inquire upon the impact of process and testing parameters:** A conscious effort was made to maintain printing parameters and testing conditions as constant as possible throughout this work. However, research indicates that some mechanical properties, such as the tensile strength, are sensitive to processing parameters and testing speeds, while others like the compressive strength remain mostly unchanged. In terms of the failure surface, this would imply that some parameters could potentially be constants, which could greatly reduce the amount of work necessary to construct a failure envelope. Additionally, literature regarding the mechanical properties of FFF parts under shear stresses is nearly non-existent at the moment, so further developments in this area could prove highly beneficial to the field.

- **Expand upon the probabilistic approach:** Sample production proved to be the most important bottleneck in this work. Torsion samples took on average two and a half hours to produce, requiring constant supervision of the robotic printer. This meant that in certain scenarios, sample sizes were relatively small for more serious statistical analysis. While the surface developed in this approach was calculated using average strength values, some sample populations were small enough to deter the application of safety factors in the form of confidence intervals based upon multiples of standard deviations. This could be solved by producing larger sample sizes once the difficulties associated with part production are resolved.

Bibliography

- [1] Ian Gibson, David Rosen, and Brent Stucker. *Additive Manufacturing Technologies*. 2nd Ed. Springer, 2015. ISBN: 978-1-4939-2112-6. DOI: [10.1007/978-1-4939-2113-3](https://doi.org/10.1007/978-1-4939-2113-3). URL: <http://link.springer.com/10.1007/978-1-4939-2113-3>.
- [2] G A Mazzei Capote, A Redmann, C Koch, and N Rudolph. “Towards a Robust Production of FFF End-User Parts with Improved Tensile Properties”. In: *Proceedings of the 28th Annual International Solid Freeform Fabrication Symposium*. Austin, TX, 2017, pp. 507–518. URL: <http://sffsymposium.engr.utexas.edu/sites/default/files/2017/Manuscripts/TowardsaRobustProductionofFFFEnderUserParts.pdf>.
- [3] Cole Hartman and Veronica de la Rosa. *Benefits of 3D Printing Vacuum Form Molds*. 2014. URL: <http://studiofathom.com/wp-content/uploads/Vacuum-Forming-White-Paper-F001-5-1-2014.pdf> (visited on 02/06/2018).
- [4] Luke Van Hulle. “Robotic Off-Axis Fused Filament Fabrication”. Master Thesis. University of Wisconsin-Madison, 2017.
- [5] Caspar de Vries. *Volkswagen Autoeuropa: Maximizing production efficiency with 3D printed tools, jigs, and fixtures*. 2017. URL: <https://ultimaker.com/en/stories/43969-volkswagen-autoeuropa-maximizing-production-efficiency-with-3d-printed-tools-jigs-and-fixtures> (visited on 02/02/2018).
- [6] Carsten Koch, Luke Van Hulle, and Natalie Rudolph. “Investigation of mechanical anisotropy of the fused filament fabrication process via customized tool path generation”. In: *Additive Manufacturing* 16 (2017), pp. 138–145. ISSN: 22148604. DOI: [10.1016/j.addma.2017.06.003](https://doi.org/10.1016/j.addma.2017.06.003). URL: <http://dx.doi.org/10.1016/j.addma.2017.06.003>.
- [7] Behzad Rankouhi, Sina Javadpour, Fereidoon Delfanian, and Todd Letcher. “Failure Analysis and Mechanical Characterization of 3D Printed ABS With Respect to Layer Thickness and Orientation”. In: *Journal of Failure Analysis and Prevention* 16.3 (2016), pp. 467–481. ISSN: 15477029. DOI: [10.1007/s11668-016-0113-2](https://doi.org/10.1007/s11668-016-0113-2).

- [8] 3D Systems. *Our Story*. 2017. URL: <https://www.3dsystems.com/our-story> (visited on 02/15/2018).
- [9] Stratasys. *About us*. 2017. URL: <http://www.stratasys.com/corporate/about-us> (visited on 02/15/2018).
- [10] ASTM International and International Organization for Standardization. *ISO/ASTM 52900:2015-Standard Terminology for Additive Manufacturing- General Principles-Terminology*. West Conshohocken, 2015. URL: <https://www.astm.org/Standards/ISOASTM52900.htm>.
- [11] 3D Hubs. *What is 3D Printing?- The definitive guide to additive manufacturing*. 2018. URL: <https://www.3dhubs.com/what-is-3d-printing{\#}technologies> (visited on 02/26/2018).
- [12] Martin Baumers, Phill Dickens, Chris Tuck, and Richard Hague. “The cost of additive manufacturing: Machine productivity, economies of scale and technology-push”. In: *Technological Forecasting and Social Change* 102 (2016), pp. 193–201. ISSN: 00401625. DOI: [10.1016/j.techfore.2015.02.015](https://doi.org/10.1016/j.techfore.2015.02.015). URL: <http://dx.doi.org/10.1016/j.techfore.2015.02.015>.
- [13] Brett P. Conner, Guha P. Manogharan, Ashley N. Martof, Lauren M. Rodomsky, Caitlyn M. Rodomsky, Dakesha C. Jordan, and James W. Limperos. “Making sense of 3-D printing: Creating a map of additive manufacturing products and services”. In: *Additive Manufacturing* 1 (2014), pp. 64–76. ISSN: 22148604. DOI: [10.1016/j.addma.2014.08.005](https://doi.org/10.1016/j.addma.2014.08.005). URL: <http://dx.doi.org/10.1016/j.addma.2014.08.005>.
- [14] Barry Berman. “3-D printing: The new industrial revolution”. In: *Business Horizons* 55.2 (2012), pp. 155–162. ISSN: 00076813. DOI: [10.1016/j.bushor.2011.11.003](https://doi.org/10.1016/j.bushor.2011.11.003). URL: <http://dx.doi.org/10.1016/j.bushor.2011.11.003>.
- [15] GE Additive. *GE Additive Manufacturing in Alabama: The Future Is Now*. 2016. URL: <https://www.ge.com/additive/press-releases/ge-additive-manufacturing-alabama-future-now> (visited on 03/01/2018).
- [16] New Balance. *The Future of Running is Here*. 2016. URL: <https://www.newbalance.com/article?id=4041> (visited on 03/07/2018).
- [17] Michelle Matisons. *Futurecraft 3D: Adidas Says It Will Turn to 3D Printed Shoes in Near Future*. 2015. URL: <https://3dprint.com/99620/futurecraft-3d-adidas-shoes/> (visited on 03/07/2018).
- [18] Sarah Saunders. *adidas and Carbon Announce Partially 3D Printed AlphaEDGE 4D LTD Shoe*. 2018. URL: <https://www.3dprint.com/203543/adidas-carbon-alphaedge-4d-ltd/> (visited on 03/07/2018).

- [19] Sung Hoon Ahn, Michael Montero, Dan Odell, Shad Roundy, and Paul K. Wright. “Anisotropic material properties of fused deposition modeling ABS”. In: *Rapid Prototyping Journal* 8.4 (2002), pp. 248–257. ISSN: 1355-2546. DOI: [10.1108/13552540210441166](https://doi.org/10.1108/13552540210441166). URL: <http://www.emeraldinsight.com/doi/10.1108/13552540210441166>.
- [20] C. S. Lee, S. G. Kim, H. J. Kim, and S. H. Ahn. “Measurement of anisotropic compressive strength of rapid prototyping parts”. In: *Journal of Materials Processing Technology* 187-188 (2007), pp. 627–630. ISSN: 09240136. DOI: [10.1016/j.jmatprotec.2006.11.095](https://doi.org/10.1016/j.jmatprotec.2006.11.095).
- [21] Paul V. Osswald and Tim A. Osswald. “A strength tensor based failure criterion with stress interactions”. In: *Polymer Composites* (2017). ISSN: 15480569. DOI: [10.1002/pc.24275](https://doi.org/10.1002/pc.24275). arXiv: [1206.4529](https://arxiv.org/abs/1206.4529). URL: <http://onlinelibrary.wiley.com/doi/10.1002/pc.24275/full> <https://doi.wiley.com/10.1002/pc.24275>.
- [22] Paul Osswald. “Comparison of Failure Criteria of Fiber Reinforced Polymer Composites”. Term Thesis. Technische Universität München, 2015.
- [23] C.T. Sun, B.J. Quinn, and J. Tao. “Comparative Evaluation of Failure Analysis Methods for Composite Laminates.” In: *U.S. Department of Transportation - May* (1996), p. 133. URL: <http://trid.trb.org/view.aspx?id=523207>.
- [24] I.I Gol'denblat and V.A. Kopnov. “Strength of Glass-Reinforced Plastics in the Complex Stress State”. In: *Mekhanika Polimerov* 1.2 (1965), pp. 70–78.
- [25] P. Obst, M. Launhardt, D. Drummer, P.V. Osswald, and T.A. Osswald. “Failure criterion for PA12 SLS additive manufactured parts”. In: *Additive Manufacturing* 21.March (2018), pp. 619–627. ISSN: 22148604. DOI: [10.1016/j.addma.2018.04.008](https://doi.org/10.1016/j.addma.2018.04.008). URL: <http://linkinghub.elsevier.com/retrieve/pii/S221486041830099X>.
- [26] P. Obst, M. Launhardt, D. Drummer, P. V. Osswald, and T. A. Osswald. “FAILURE CRITERION FOR SLS ADDITIVE MANUFACTURED PARTS”. In: *SPE ANTEC(R) Anaheim 2017*. Anaheim, 2017, pp. 49–54.
- [27] SABIC. *SABIC Cycloc MG94 Datasheet*. 2016.
- [28] Lulzbot. *TAZ 5*. 2018. URL: <https://www.lulzbot.com/store/printers/lulzbot-taz-5>.
- [29] ASTM International. “Standard test method for tensile properties of plastics”. In: *ASTM International* 08 (2014), pp. 46–58. DOI: [10.1520/D0638-14.1](https://doi.org/10.1520/D0638-14.1). URL: [http://scholar.google.com/scholar?hl=en&btnG=Search&q=intitle:Standard+Test+Method+for+Tensile+Properties+of+Plastics%20](https://scholar.google.com/scholar?hl=en&btnG=Search&q=intitle:Standard+Test+Method+for+Tensile+Properties+of+Plastics%20).
- [30] Luke Van Hulle. *SciSlice- The Scientific Slicer*. 2017. URL: <https://github.com/VanHulleOne/SciSlice>.

-
- [31] G.P. Zaitsev, V.A. Pashkov, and V.S. Strelyaeve. “Probabilistic Evaluation of the Criteria of Static Strength of Reinforced Plastics”. In: *Problemy Prochnosti* 8 (1975), pp. 3–9.

A SABIC Cycloc MG94 Datasheet

Reproduced from SABIC's Datasheet Document [27].

Superior flow, injection molding ABS. Good impact. For thin-wall applications.

TYPICAL PROPERTIES ¹	TYPICAL VALUE	Unit	Standard
MECHANICAL			
Tensile Stress, yld, Type I, 5 mm/min	460	kgf/cm ²	ASTM D 638
Tensile Stress, brk, Type I, 5 mm/min	350	kgf/cm ²	ASTM D 638
Tensile Strain, yld, Type I, 5 mm/min	2	%	ASTM D 638
Tensile Strain, brk, Type I, 5 mm/min	18	%	ASTM D 638
Tensile Modulus, 5 mm/min	25200	kgf/cm ²	ASTM D 790
Flexural Stress, yld, 1.3 mm/min, 50 mm span	800	kgf/cm ²	ASTM D 790
Flexural Modulus, 1.3 mm/min, 50 mm span	26700	kgf/cm ²	ASTM D 790
Hardness, Rockwell R	113	-	ASTM D 785
Tensile Stress, yield, 50 mm/min	46	MPa	ISO 527
Tensile Stress, break, 50 mm/min	35	MPa	ISO 527
Tensile Strain, yield, 50 mm/min	2.3	%	ISO 527
Tensile Strain, break, 50 mm/min	40	%	ISO 527
Tensile Modulus, 1 mm/min	2450	MPa	ISO 527
Flexural Stress, yield, 2 mm/min	70	MPa	ISO 178
Flexural Modulus, 2 mm/min	2500	MPa	ISO 178
IMPACT			
Izod Impact, notched, 23°C	24	cm-kgf/cm	ASTM D 256
Izod Impact, notched, -30°C	8	cm-kgf/cm	ASTM D 256
Instrumented Impact Total Energy, 23°C	214	cm-kgf	ASTM D 3763
Instrumented Impact Total Energy, -30°C	50	cm-kgf	ASTM D 3763
Izod Impact, notched 80°10°4 +23°C	16	kJ/m ²	ISO 180/1A
Izod Impact, notched 80°10°4 -30°C	7	kJ/m ²	ISO 180/1A

TYPICAL PROPERTIES ¹	TYPICAL VALUE	Unit	Standard
IMPACT			
Charpy 23°C, V-notch Edgew 80*10*4 sp=62mm	18	kJ/m ²	ISO 179/1eA
 THERMAL			
Vicat Softening Temp, Rate B/50	98	°C	ASTM D 1525
HDT, 0.45 MPa, 3.2 mm, unannealed	95	°C	ASTM D 648
HDT, 1.82 MPa, 3.2mm, unannealed	82	°C	ASTM D 648
CTE, -40°C to 40°C, flow	8.82E-05	1/°C	ASTM E 831
CTE, -40°C to 40°C, xflow	8.46E-05	1/°C	ASTM E 831
CTE, -40°C to 40°C, flow	8.82E-05	1/°C	ISO 11359-2
CTE, -40°C to 40°C, xflow	8.46E-05	1/°C	ISO 11359-2
Vicat Softening Temp, Rate B/50	98	°C	ISO 306
Vicat Softening Temp, Rate B/120	100	°C	ISO 306
HDT/Be, 0.45MPa Edgew 120*10*4 sp=100mm	89	°C	ISO 75/Be
HDT/Ae, 1.8 MPa Edgew 120*10*4 sp=100mm	76	°C	ISO 75/Ae
Relative Temp Index, Elec	60	°C	UL 746B
Relative Temp Index, Mech w/impact	60	°C	UL 746B
Relative Temp Index, Mech w/o impact	60	°C	UL 746B
PHYSICAL			
Specific Gravity	1.05	-	ASTM D 792
Mold Shrinkage, flow, 3.2 mm (5)	0.5 - 0.8	%	SABIC Method
Melt Flow Rate, 230°C/3.8 kgf	11.7	g/10 min	ASTM D 1238
Melt Viscosity, 240°C, 1000 sec-1	1720	poise	ASTM D 3825
Density	1.04	g/cm ³	ISO 1183
Melt Flow Rate, 220°C/5.0 kg	12	g/10 min	ISO 1133
Melt Flow Rate, 220°C/10.0 kg	42	g/10 min	ISO 1133
FLAME CHARACTERISTICS			
UL Recognized, 94HB Flame Class Rating (3)	1.52	mm	UL 94

CYCOLAC™ Resin MG94

Americas: COMMERCIAL

PROCESSING PARAMETERS	TYPICAL VALUE	Unit
Injection Molding		
Drying Temperature	80 - 90	°C
Drying Time	2 - 4	hrs
Drying Time (Cumulative)	8	hrs
Maximum Moisture Content	0.1	%
Melt Temperature	205 - 245	°C
Nozzle Temperature	205 - 245	°C
Front - Zone 3 Temperature	205 - 225	°C
Middle - Zone 2 Temperature	200 - 210	°C
Rear - Zone 1 Temperature	190 - 200	°C
Mold Temperature	50 - 70	°C
Back Pressure	0.3 - 0.7	MPa
Screw Speed	30 - 60	rpm
Shot to Cylinder Size	50 - 70	%
Vent Depth	0.038 - 0.051	mm

B Failure Surface Code

```

1 %
2 %           FFF failure surface
3 %           Developed by Gerardo A. Mazzei Capote
4 %           Based on findings by T. Osswald, P.V. Osswald and P. Obst
5 %           March 2018
6 %
7 %Failure Criterion proposed by P.V. Osswald and T.A. Osswald.
8 %For more information, refer to:
9 %Journal of Polymer Composites, DOI 10.1002/pc.24275
10 %The notation here follows the same notation used in this paper
11 %
12 classdef FailSurf
13     methods (Static)
14         function [F_11,F_1111,F_22,F_2222,F_12,F_1212,F_1122,F_1112,F_2212]=tens(Xt,Xc,Yt,Yc,S,S45_p,S45_n,
15             mu1112,mu2212,lambda1122) %Tensorial components calculation
16             F_1111=0.25*(1/Xt+1/Xc)^2;
17             F_2222=0.25*(1/Yt+1/Yc)^2;
18             F_1212=(1/S)^2;
19             F_11=0.5*(1/Xt-1/Xc);
20             F_22=0.5*(1/Yt-1/Yc);
21             F_12=0;
22             %Flexibility regarding which slope to use:
23             disp('0- Goldenblat-Kopnov, 1- Positive x axis, 2- Negative x axis, 4-
24                 Negative y axis')
25             reply = input('Please enter which slope option corresponds to lambda: ');
26             if reply == 0
27                 F_1122=0.125*((1/Xt+1/Xc)^2+(1/Yt+1/Yc)^2-(1/S45_p+1/S45_n)^2); %Per Gol'denblat- Kopnov
28             elseif reply == 1
29                 F_1122=-((F_11+F_22*lambda1122)*F_1111^0.5+F_1111)/lambda1122; %Slope at Intercept of
30                 Positive x axis
31             elseif reply == 2
32                 F_1122=-(F_11-F_22*lambda1122)*F_2222^0.5-F_2222*lambda1122; %Slope at Intercept of Positive
33                 y axis
34             elseif reply == 3
35                 F_1122=((F_11+F_22*lambda1122)*F_1111^0.5-F_1111)/lambda1122; %Slope at Intercept of
36                 Negative x axis
37             elseif reply == 4
38                 F_1122=(F_11+F_22*lambda1122)*F_2222^0.5-F_2222*lambda1122; %Slope at Intercept of Negative
39                 y axis
40             else
41                 error('Input must be one of the options listed above. Execution ended.')
42             end
43             F_1112=-(F_11/S)-F_1212*mu1112;
44             F_2212=-(F_22/S)-F_1212*mu2212;
45         end
46         %%
47         function f=criteria(s1,s2,t12,F_11,F_1111,F_22,F_2222,F_12,F_1212,F_1122,F_1112,F_2212) %Evaluating
48             %the failure criteria for stress inputs
49             %s1: sigma11, s2: sigma22, t12: tau12
50             f=F_11*s1+F_22*s2+F_12*t12+...

```

```

44      ( $F_{1111}s_1^2 + F_{2222}s_2^2 + 2F_{1122}s_1s_2 + F_{1212}s_1t_{12}^2 + 2F_{2212}s_2|abs(t_{12}) + 2F_{1112}s_1s_2$ ) *  

45      abs(t_{12}))^.5;
46  for x=1:size(f) %Filter any results where f is greater than 1
47    if f(x)>1
48      f(x)=1;
49    end
50  end
51 %%
52 function g=graph(s1,s2,t12,f,s) %Used to plot the resulting failure surface
53   %s: number of equally spaced failure surfaces from 0 to 1
54   %e.g. s=5 will generate 4 surfaces: 0.25, 0.5, 0.75 and 1
55   if nargin ==4)
56     s= 5;
57     disp('Using f from 0 to 1 in increments of 0.25 by default')
58   end
59   cvals = linspace(0,1,s);
60   Sx = []; Sy = []; Sz = -70:70;
61   g=figure(1); %Create new figure
62   contourslice(s1,s2,t12,f,Sx,Sy,Sz,cvals);
63   view(3); %View angle
64   axis tight; %Set axes
65   daspect([1,1,1]); %data aspect ratio of 1:1:1
66   box on %encloses all plot
67   set(gca,'FontSize',14) %Sets the font size for axes
68   hold on
69   xlabel('\sigma_{11} [MPa]', 'fontsize',16) % x-axis label
70   ylabel('\sigma_{22} [MPa]', 'fontsize',16) % y-axis label
71   zlabel('\tau_{12} [MPa]', 'fontsize',16) % z-axis label
72   %Allow user to save graph
73   reply1 = input('Would you like to save this graph? [Y/N]: ', 's');
74   if isempty(reply1)
75     reply1 = 'N';
76     disp('No input. Using "N" as default')
77   end
78   if (reply1=='Y')
79     disp('Available options: -dpdf, -depsc, -dpng, -djpeg')
80     reply2= input('Select file type: ', 's');
81     if isempty(reply2)
82       reply2 = '-djpeg';
83       disp('No input. Graph saved as jpeg by default.')
84     end
85     reply3= input('Choose file name : ', 's');
86     if isempty(reply3)
87       reply3 = 'fig1';
88       disp('No input. Graph named "fig1" by defalut.')
89     end
90     print(reply3,reply2) %Saves plot in selected file type on the current directory
91   elseif (reply1== 'N')
92     disp('Graph not saved.')
93   else
94     error('Input must be one of the options listed above. Execution ended.')
95   end
96 end
97 end
98 end

```

C Failure Surface Data

```

1 %Initialize data
2
3 %0 deg orientation
4
5 %Tensile data
6 X_t=[40.172 39.538 39.367 39.91 39.837 39.911 39.584 39.968 39.802 40.79...
7 41.259 40.385 39.554 40.245 40.032 41.666 41.899 40.286 41.263]';
8
9 SX_t=length(X_t);
10 x_t=zeros(SX_t,3);
11 x_t(:,1)=X_t; %Array in format (sigma_{11},sigma_{22},tau_{12})
12
13 %Compression data
14 X_c=[-48.54147 47.00401 46.12378 44.59113 44.9143 46.58337 42.28337...
15 47.71981 44.01373 42.2326 39.92783 46.67828 44.07402 44.80455...
16 44.08797 44.39603 46.00331 39.11883 48.86942 37.9517 39.34137...
17 45.79583 39.51087 44.65304 38.45435]';
18
19 SX_c=length(X_c);
20 x_c=zeros(SX_c,3);
21 x_c(:,1)=X_c; %Array in format (sigma_{11},sigma_{22},tau_{12})
22
23 %Shear data
24
25 %Pure shear
26 S_0=[18.52085535 26.06958269 23.22084951 23.38504379...
27 20.8072288 22.46146189 25.7781399 26.56626146];
28 SS_0=length(S_0);
29 s_0=zeros(SS_0,3);
30 s_0(:,3)=S_0;
31
32 %Combined load
33
34 %Shear-Compression
35 S_0c=[18.14731942 23.86530388 18.34845298 24.65342294 25.10906001...
36 26.27892459 23.67238066 21.82521935 21.73491412 27.6663504]';
37 SS_0c=length(S_0c);
38 s_0c=zeros(SS_0c,3);
39 s_0c(:,3)=S_0c;
40 s_0c(:,1)=-5.8; %Average compressive stress
41
42 S_0t=[19.02574471 22.77342677 25.65499481 26.46364347 23.72984603...
43 25.61805403 22.63796893 21.10687843]'; %Shear-Tension
44 SS_0t=length(S_0t);
45 s_0t=zeros(SS_0t,3);
46 s_0t(:,3)=S_0t;
47 s_0t(:,1)=5.8; %Average Tensile stress
48
49 %
50 %90 deg orientation

```

```

51
52 %Tensile data
53 Y_t=[31.64 30.97 31.13 31.32 30.77 31.42 31.01 31.29 30.94 29.68...
54     31.35 32.08]';
55
56 SY_t=length(Y_t);
57 y_t=zeros(SY_t,3);
58 y_t(:,2)=Y_t; %Array in format (sigma_{11},sigma_{22},tau_{12})
59
60 %Compressive data
61 Y_c=[58.92928 58.31638 58.64349 55.45486 59.14833 55.81437...
62     55.26091 58.68458 59.45549 58.46141 58.97464 56.58839...
63     56.95103 54.93245 58.98146 56.47761 56.37775 61.38843...
64     58.7201 58.5109 61.1229]';
65
66 SY_c=length(Y_c);
67 y_c=zeros(SY_c,3);
68 y_c(:,2)=Y_c; %Array in format (sigma_{11},sigma_{22},tau_{12})
69
70 %Shear data
71 S_90=[26.26661183 26.155782 18.93133605 25.6303668 25.06801081...
72     18.270463 24.14443141 19.92059117 23.0936035 26.59910131]'; %Pure shear
73 SS_90=length(S_90);
74 S_90=zeros(SS_90,3);
75 S_90(:,3)=S_90;
76
77 %Combined load
78 S_90c=[20.4295892 20.88932469 23.87762039 18.57011338 23.96381845...
79     24.32504187 24.05002026 26.50058674 20.97142058]'; %Shear-Compression
80 SS_90c=length(S_90c);
81 S_90c=zeros(SS_90c,3);
82 S_90c(:,3)=S_90c;
83 S_90c(:,2)=-5.8; %Average compressive stress
84
85 %Shear-Tension
86 S_90t=[22.87582762 21.82002019 21.35826044 18.32312608 16.36626314...
87     19.00453371 19.26411757 23.93413104 21.6028683 23.40997133]';
88 SS_90t=length(S_90t);
89 S_90t=zeros(SS_90t,3);
90 S_90t(:,3)=S_90t;
91 S_90t(:,2)=5.8; %Average Tensile stress

```

D Surface Plots

```

1 %Failure Surface plots
2 clear all
3 clc
4 test =4; %Change number to calculate desired surface
5 if (test==1)
6 %G. Mazzei Master Thesis; 11–22 plane
7 Xt=40.29; Xc=43.91; Yt=31.13; Yc=57.96; S=23.35;
8 S45p=20.80; S45n=38.17; mu1=-0.0052; mu2=-0.2; lambda=0;
9 x=-70:0.5:50;
10 y=-70:0.5:40;
11 t12=0;
12 [s1,s2]=meshgrid(x,y);
13 [F_11,F_1111,F_22,F_2222,F_12,F_1212,F_1122,F_1112,F_2212]=FailSurf.tens(Xt,Xc,Yt,Yc,S,S45p,S45n,mu1,mu2
    ,lambda);
14 f=FailSurf.criteria(s1,s2,t12,F_11,F_1111,F_22,F_2222,F_12,F_1212,F_1122,F_1112,F_2212);
15 g=contour(s1,s2,f,[1,1],'-k');
16 hold on
17 box on
18 grid on
19 axis tight
20 daspect([1,1,1]); %data aspect ratio of 1:1
21 xlabel('\sigma_{11} [MPa]', 'FontSize', 18) % x-axis label
22 ylabel('\sigma_{22} [MPa]', 'FontSize', 18) % y-axis label
23 set(gca, 'FontSize', 16) %Sets the font size for axes
24 set(gca, 'FontName', 'CMU Serif') %Sets the font size for axes
25 h=contour(s1,s2,f,[1,0.75],'-k');
26 i=contour(s1,s2,f,[1,0.5],'-k');
27 j=contour(s1,s2,f,[1,0.25],':k');
28 % clabel(g,'manual','FontName','CMU Serif', 'FontSize', 14)
29 clabel([g h i j],'manual','FontName','CMU Serif', 'FontSize', 14)
30 %User selected marker location for f values
31 Data_summary %load data
32 xL = xlim;
33 yL = ylim;
34 line([0 0], yL,'Color','k'); %x-axis
35 line(xL, [0 0],'Color','k'); %y-axis
36 plot(x_c(:,1),x_c(:,2),'r.', 'MarkerSize',20);
37 plot(x_t(:,1),x_t(:,2),'r.', 'MarkerSize',20);
38 plot(y_c(:,1),y_c(:,2),'r.', 'MarkerSize',20);
39 plot(y_t(:,1),y_t(:,2),'r.', 'MarkerSize',20);
40 elseif (test==2)
41 %G. Mazzei Master Thesis; 11–12 plane
42 Xt=40.29; Xc=43.91; Yt=31.13; Yc=57.96; S=23.35;
43 S45p=20.80; S45n=38.17; mu1112=-0.0052; mu2212=-0.2;
44 lambda=-0.51;
45 x=-50:0.5:50;
46 y=0:0.5:30;
47 s2=0;
48 [s1,t12]=meshgrid(x,y);
49 [F_11,F_1111,F_22,F_2222,F_12,F_1212,F_1122,F_1112,F_2212]=FailSurf.tens(Xt,Xc,Yt,Yc,S,S45p,S45n,mu1112,

```

```

    mu2212,lambda);
50 f=FailSurf.criteria(s1,s2,t12,F_11,F_1111,F_22,F_2222,F_12,F_1212,F_1122,F_1112,F_2212);
51 g=contour(s1,t12,f,[1,1],'-k');
52 hold on
53 box on
54 grid on
55 axis tight
56 daspect([1,1,1]); %data aspect ratio of 1:1
57 xlabel('\sigma_{11} [MPa]', 'fontsize',18) % x-axis label
58 ylabel('\tau_{12} [MPa]', 'fontsize',18) % y-axis label
59 set(gca,'FontSize',16) %Sets the font size for axes
60 set(gca,'FontName','CMU Serif') %Sets the font size for axes
61 h=contour(s1,t12,f,[1,0.75],'-k');
62 i=contour(s1,t12,f,[1,0.5],'-k');
63 j=contour(s1,t12,f,[1,0.25],':k');
64 clabel([g h i j], 'manual', 'FontName', 'CMU Serif', 'FontSize', 14)
65 %User selected marker location for f values
66 Data_summary %load data
67 xL = xlim;
68 yL = ylim;
69 line([0 0], yL,'Color','k'); %x-axis
70 line(xL, [0 0],'Color','k'); %y-axis
71 xslope = [10 -10];
72 yslope = [23.2980 23.4020];
73 line(xslope,yslope,'Color',[0.4 0 0], 'LineStyle', '--', 'LineWidth',2)
74 plot(x_c(:,1),x_c(:,3),'r.', 'MarkerSize',20);
75 plot(x_t(:,1),x_t(:,3),'r.', 'MarkerSize',20);
76 plot(s_0(:,1),s_0(:,3),'r.', 'MarkerSize',20);
77 plot(s_0c(:,1),s_0c(:,3),'r.', 'MarkerSize',20);
78 plot(s_0t(:,1),s_0t(:,3),'r.', 'MarkerSize',20);
79
80 elseif (test==3)
81 %G. Mazzei Master Thesis; 22-12 plane
82 Xt=40.29; Xc=43.91; Yt=31.13; Yc=57.96; S=23.35;
83 S45p=20.80; S45n=38.17; mu1112=-0.0052; mu2212=-0.2;
84 lambda=0;
85 x=-70:0.5:40;
86 y=0:0.5:30;
87 s1=0;
88 [s2,t12]=meshgrid(x,y);
89 [F_11,F_1111,F_22,F_2222,F_12,F_1212,F_1122,F_1112,F_2212]=FailSurf.tens(Xt,Xc,Yt,Yc,S,S45p,S45n,mu1112,
    mu2212,lambda);
90 f=FailSurf.criteria(s2,s2,t12,F_11,F_1111,F_22,F_2222,F_12,F_1212,F_1122,F_1112,F_2212);
91 g=contour(s2,t12,f,[1,1],'-k');
92 hold on
93 box on
94 grid on
95 axis tight
96 daspect([1,1,1]); %data aspect ratio of 1:1
97 xlabel('\sigma_{22} [MPa]', 'fontsize',18) % x-axis label
98 ylabel('\tau_{12} [MPa]', 'fontsize',18) % y-axis label
99 set(gca,'FontSize',16) %Sets the font size for axes
100 set(gca,'FontName','CMU Serif') %Sets the font size for axes
101 h=contour(s2,t12,f,[1,0.75],'-k');
102 i=contour(s2,t12,f,[1,0.5],'-k');
103 j=contour(s2,t12,f,[1,0.25],':k');
104 clabel([g h i j], 'manual', 'FontName', 'CMU Serif', 'FontSize', 14)
105 %User selected marker location for f values
106 Data_summary %load data
107 xL = xlim;
108 yL = ylim;
109 line([0 0], yL,'Color','k'); %x-axis
110 line(xL, [0 0],'Color','k'); %y-axis
111 xslope = [10 -10];
112 yslope = [21.41 25.4100];

```

```
113 line(xslope,yslope,'Color',[0.4 0 0],'LineStyle','—','LineWidth',2)
114 plot(y_c(:,2),y_c(:,3),'r.','MarkerSize',20);
115 plot(y_t(:,2),y_t(:,3),'r.','MarkerSize',20);
116 plot(s_90(:,2),s_90(:,3),'r.','MarkerSize',20);
117 plot(s_90c(:,2),s_90c(:,3),'r.','MarkerSize',20);
118 plot(s_90t(:,2),s_90t(:,3),'r.','MarkerSize',20);
119
120 elseif (test==4)
121 %G. Mazzei Master Thesis; Full surface
122 Xt=40.29; Xc=43.91; Yt=31.13; Yc=57.96; S=23.35;
123 S45p=20.80; S45n=38.17; mu1112=-0.0052; mu2212=-0.2;
124 lambda=0;
125 x=-80:0.5:80;
126 y=-80:0.5:80;
127 z=0:0.5:80;
128 [s1,s2,t12]=meshgrid(x,y,z);
129 [F_11,F_1111,F_22,F_2222,F_12,F_1212,F_1122,F_1112,F_2212]=FailSurf.tens(Xt,Xc,Yt,Yc,S,S45p,S45n,mu1112,
    mu2212,lambda);
130 f=FailSurf.criteria(s1,s2,t12,F_11,F_1111,F_22,F_2222,F_12,F_1212,F_1122,F_1112,F_2212);
131 g=FailSurf.graph(s1,s2,t12,f);
132 hold on
133 box on
134 grid on
135 axis tight
136 daspect([1,1,1]); %data aspect ratio of 1:1
137 end
```